Cancer Cell

Article

Integrative molecular and spatial analysis reveals evolutionary dynamics and tumor-immune interplay of *in situ* and invasive acral melanoma

Graphical abstract

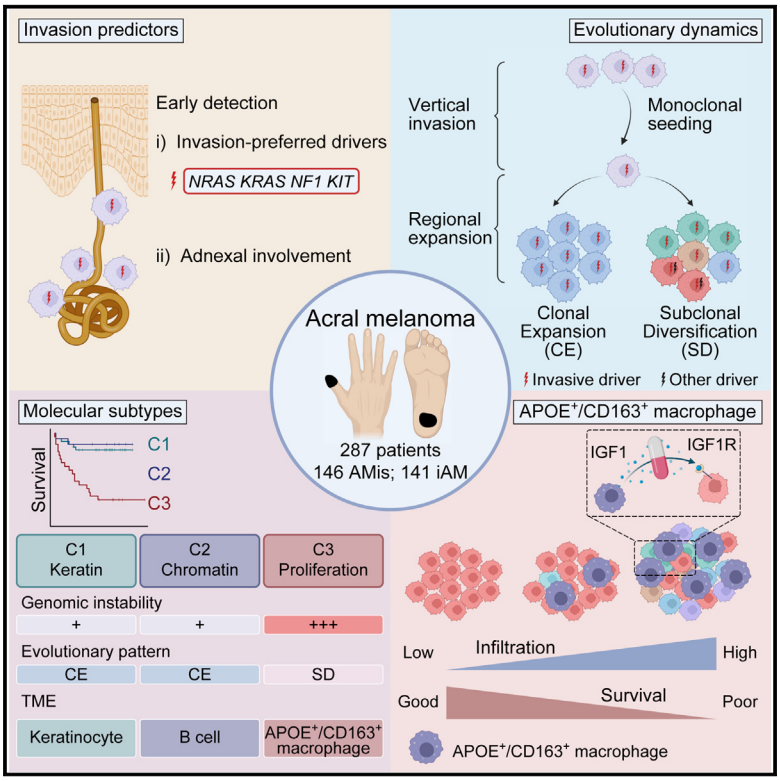

Highlights

- Invasion-preferred drivers and adnexal involvement predict early invasion of AMis
- Subclonal diversification accelerates the regional expansion of iAM
- APOE$^+$/CD163$^+$ macrophages promote tumor EMT via IGF1-IGF1R interaction
- APOE and CD163 staining is a prognostic biomarker for AM

Authors

Hengkang Liu, Jiawen Gao, Mei Feng, ..., Ruidong Xue, Ning Zhang, Hang Li

Correspondence

rxue@hsc.pku.edu.cn (R.X.), zhangning@bjmu.edu.cn (N.Z.), drlihang@126.com (H.L.)

In brief

Integrating six omics datasets, Liu et al. dissect the evolutionary dynamics and spatial architecture of early-stage AM. They demonstrate that APOE$^+$/CD163$^+$ macrophages promote tumor EMT via IGF1-IGF1R interaction in a subset of iAM patients exhibiting subclonal diversification and poor prognosis, which provides a potential therapeutic target.

Liu et al., 2024, Cancer Cell *42*, 1067–1085
June 10, 2024
https://doi.org/10.1016/j.ccell.2024.04.012

CellPress

Cancer Cell

CellPress
OPEN ACCESS

Article

Integrative molecular and spatial analysis reveals evolutionary dynamics and tumor-immune interplay of *in situ* and invasive acral melanoma

Hengkang Liu,[1,2,6] Jiawen Gao,[3,4,6] Mei Feng,[1,6] Jinghui Cheng,[1] Yuchen Tang,[3] Qi Cao,[1] Ziji Zhao,[1] Ziqiao Meng,[1] Jiarui Zhang,[3] Guohong Zhang,[3] Chong Zhang,[3] Mingming Zhao,[3] Yicen Yan,[3] Yang Wang,[3] Ruidong Xue,[1,2,*] Ning Zhang,[1,2,5,7,*] and Hang Li[1,3,5,*]

[1]Peking University-Yunnan Baiyao International Medical Research Center, Peking University First Hospital, Beijing 100191, China
[2]School of Basic Medical Sciences, International Cancer Institute, Peking University, Beijing 100191, China
[3]National Clinical Research Center for Skin and Immune Diseases, NMPA Key Laboratory for Quality Control and Evaluation of Cosmetics, Beijing Key Laboratory of Molecular Diagnosis on Dermatoses, Peking University First Hospital, Beijing 100034, China
[4]Institute of Photomedicine and Department of Phototherapy at Shanghai Skin Disease Hospital, School of Medicine, Tongji University, Shanghai 200443, China
[5]Yunnan Baiyao Group, Kunming 650500, China
[6]These authors contributed equally
[7]Lead contact
*Correspondence: rxue@hsc.pku.edu.cn (R.X.), zhangning@bjmu.edu.cn (N.Z.), drlihang@126.com (H.L.)
https://doi.org/10.1016/j.ccell.2024.04.012

SUMMARY

In acral melanoma (AM), progression from *in situ* (AMis) to invasive AM (iAM) leads to significantly reduced survival. However, evolutionary dynamics during this process remain elusive. Here, we report integrative molecular and spatial characterization of 147 AMs using genomics, bulk and single-cell transcriptomics, and spatial transcriptomics and proteomics. Vertical invasion from AMis to iAM displays an early and monoclonal seeding pattern. The subsequent regional expansion of iAM exhibits two distinct patterns, clonal expansion and subclonal diversification. Notably, molecular subtyping reveals an aggressive iAM subset featured with subclonal diversification, increased epithelial-mesenchymal transition (EMT), and spatial enrichment of $APOE^{+}/CD163^{+}$ macrophages. *In vitro* and *ex vivo* experiments further demonstrate that $APOE^{+}CD163^{+}$ macrophages promote tumor EMT via IGF1-IGF1R interaction. Adnexal involvement can predict AMis with higher invasive potential whereas APOE and CD163 serve as prognostic biomarkers for iAM. Altogether, our results provide implications for the early detection and treatment of AM.

INTRODUCTION

Acral melanoma (AM), derived from melanocytes in sun-shielded palms, soles, and nails,[1] is the major subtype of melanoma in Asians.[2] AM is often diagnosed at an advanced stage, which frequently develops metastasis and shows a dismal prognosis.[3] Early detection and prevention of AM could significantly improve patient prognosis.[4] Recent efforts have collectively portrayed the unique genomic landscape of AM.[5–9] However, these studies mainly focus on late-stage invasive AM and our understanding of early-stage AM is still very limited.

AM *in situ* (AMis) is an early-stage neoplasm manifesting atypical melanocytes confined to the epithelial layer and exhibiting a radial growth pattern.[10–12] AMis could remain in the preinvasive stage for many years, while only a small percentage of them would vertically invade the dermis, termed as vertical invasion.[13] This clinical observation indicates an evolutionary bottleneck for vertical invasion that may require additional genetic alterations.[10] After this stage, the tumor cells turn into invasive AM (iAM), and continue its progression and expansion, termed regional expansion. Therefore, elucidating the critical molecular determinants and evolutionary dynamics during vertical invasion and regional expansion may provide clues for the early detection and therapeutic intervention of AM.[14–16] However, due to the low rate of AMis at diagnosis and the low purity of such samples, the genomic landscape of AMis remains unknown and a detailed comparison with iAM is lacking.

Recent advances in immunotherapies underline the vital role of the tumor microenvironment (TME) during tumor progression.[17,18] Multi-omic analyses have revealed diverse molecular subsets of melanoma, including cutaneous melanoma (CM) and uveal melanoma (UM), which correspond to different TME subtypes and exhibit distinct responses to immunotherapies.[19–21] Several recent studies have described the immunosuppressive TME of AM at single-cell resolution.[22,23] However, how TME components contribute to AM invasion remains largely unknown.

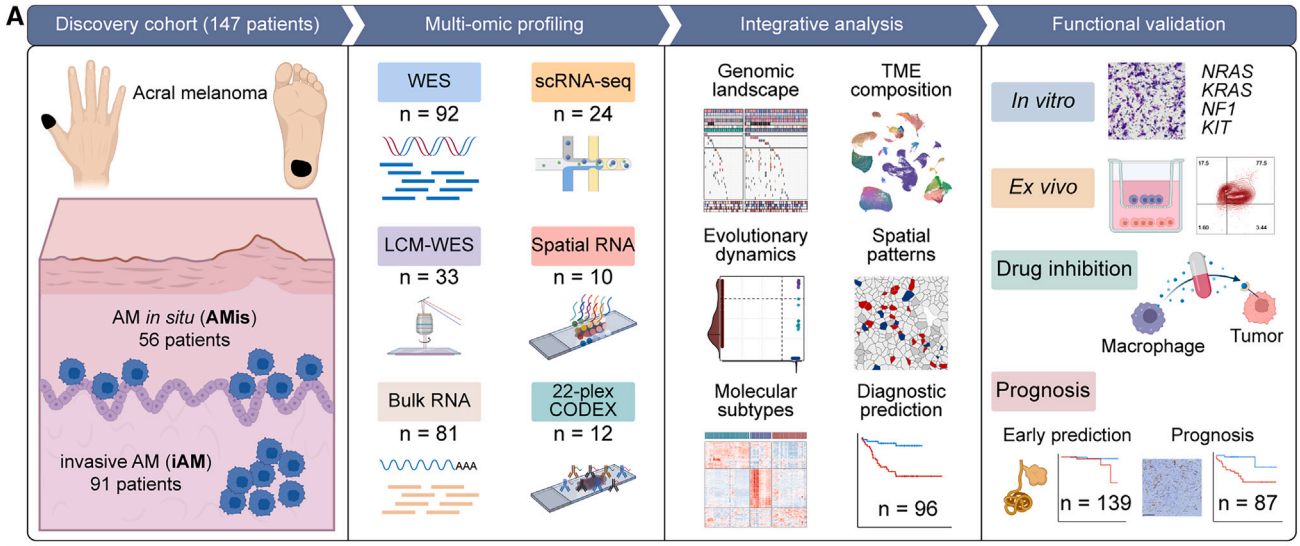

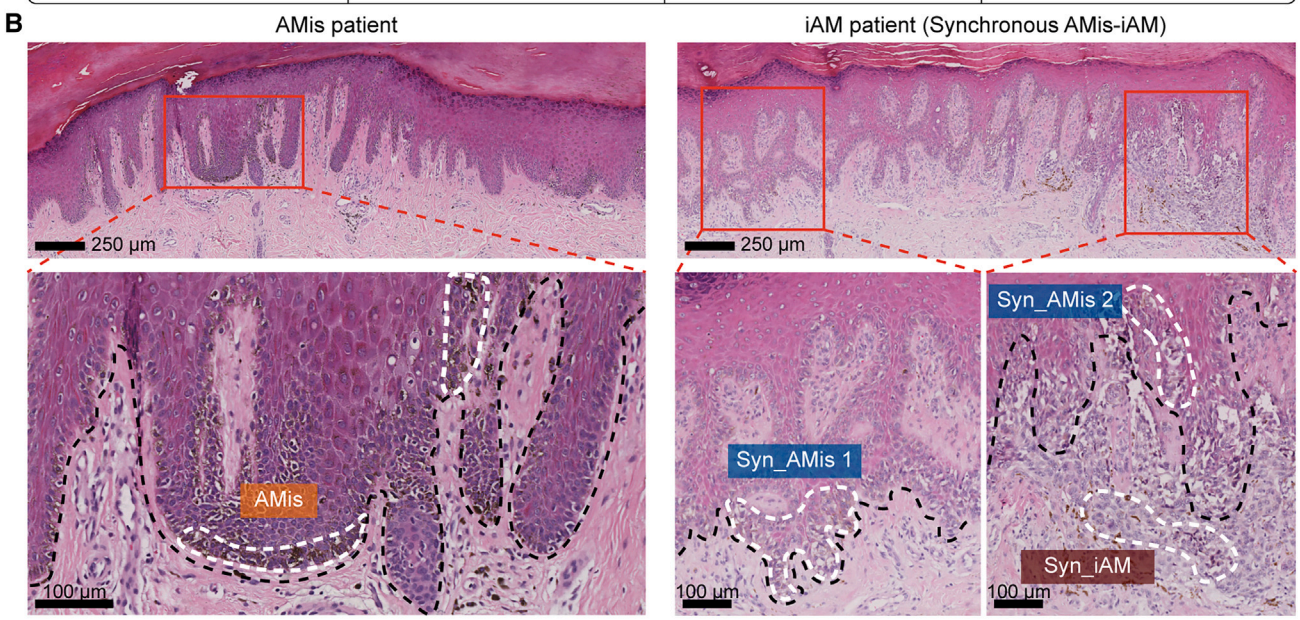

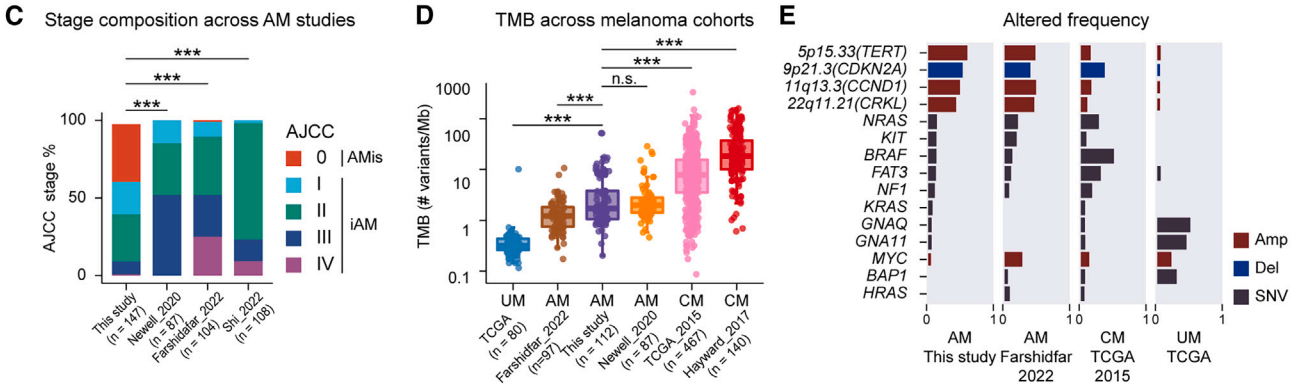

Figure 1. Research strategy and cohort information

(A) Research strategy. "*n*", sample number.

(B) Representative H&E stainings. White dashes show laser-capture microdissection regions; black dotted lines mark the basement membrane.

(C) Composition of different acral melanoma (AM) cohorts per the AJCC stage. Chi-square test.

(legend continued on next page)

To address the aforementioned issues, we assembled an AM cohort of 287 patients, containing a core discovery cohort of 147 patients and two validation cohorts of 140 patients. Among these, 146 patients and 141 patients were diagnosed as AMis and iAM, respectively. Integrative analysis of six omics datasets, including whole exome sequencing (WES), multi-region sequencing based on laser-capture microdissection (LCM), bulk RNA sequencing (RNA-seq), single-cell RNA sequencing (scRNA-seq), spatial transcriptomic sequencing, co-detection-by-indexing (CODEX), and immunohistochemistry (IHC) datasets discovered invasion predictors, delineated the evolutionary dynamics, revealed three molecular subtypes, and identified APOE^{+}CD163^{+} macrophages as a prognostic biomarker for AM. Functional experiments further demonstrated that APOE^{+}CD163^{+} macrophages could promote the epithelial-mesenchymal transition (EMT) of tumor cells via IGF1-IGF1R interaction.

RESULTS

Discovery cohort and genomic landscape

The discovery cohort contained 56 patients with AMis and 91 patients with iAM (Figures 1A and S1A–S1D, and Table S1). Patients with AMis were younger (mean = 56.9, range 29–79) than those with iAM (mean = 63.6, range 30–88; p = 0.0011; Table S1). Ulceration and adnexal involvement were present in 15% and 47% of patients, respectively (Figure S1D). Of note, many iAM tumors contain malignant cells in the epidermis manifesting as AMis lesions, and these tumors can also be termed synchronous AMis-iAM. This dual phenotype of synchronous AMis-iAM makes it an ideal model for investigating the intra-patient evolutionary dynamics of AM invasion. We applied LCM to isolate matched and high-purity tumor samples from the same patient (Figure 1B), including 12 Syn_AMis and 11 Syn_iAM regions from 12 patients. For better data comparison, we also collected 8 AMis regions from 8 pure AMis patients. Previous AM cohorts mainly focused on iAM (American Joint Committee on Cancer [AJCC] stages I–IV).[5–7] By contrast, our cohort enrolled 38% (56/147) of AMis patients (AJCC stage 0) (Figure 1C), providing us the opportunity to systematically characterize these early-stage neoplasms.

The average coverage of WES was 313×, which enabled accurate mutation calling and clonal composition reconstruction (Figure S1E). The tumor mutational burden (TMB) of our cohort (median 1.6, range 0.2–48.2) was comparable to previous AM cohorts,[6,7] higher than UM, and lower than CM (Figure 1D).[19,24] The broad copy number alteration (CNA) profile (Figures 1E and S1F–S1H) and mutational signatures of AM (Figures S1I and S1J; Table S2) were similar to those of previous AM cohorts,[5,6] yet distinct from those of CM and UM.[19] For instance, the recently reported 22q11.21 amplification could also be identified, which exhibited a consistently poor prognosis (Figure S1H).[6] These results validated the high quality of our cohort, enabling the in-depth analysis of AM invasion.

Genomic comparison of AMis and iAM identifies invasion-preferred drivers

To identify potential events driving the vertical invasion of AM, we compared the genomic landscape between AMis and iAM samples (Figures 2A, S2A, and S2B). TMB was comparable (Figure 2B), and no single mutation was significantly enriched in either AMis or iAM. Screening of gene combinations identified that the mutational frequency of four driver genes (*NRAS*, *KRAS*, *NF1*, or *KIT*) was significantly higher in iAM samples (p = 0.037; Figure 2C). This result was validated in another AM cohort (Figure S2C).[9] We termed these four genes as "invasion-preferred drivers" for AM. Induction of hotspot mutations (including *NRAS*^{Q61K}, *NRAS*^{Q61R}, *KRAS*^{G12D}, and *KIT*^{L576P}) and knock out of *NF1* independently enhanced the invasion of an AM cell line, LM-MEL-45 (Figure 2D), supporting the functional role of invasion-preferred drivers. Meanwhile, the mutational frequencies of either *BRAF* alone or in combination with the invasion-preferred drivers were comparable between the two groups (Figures S2D and S2E). This observation is consistent with the notion that *BRAF* mutation is an initial and ubiquitous driver acquired early in benign lesions.[25] Taken together, these results suggest that AM invasion is highly dependent on acquiring certain driver mutations rather than simply accumulating more mutations.

The percentage of subclonal mutations, i.e., mutations not shared by all tumor cells in a certain tumor, can assess the extent of intratumor heterogeneity (ITH). Interestingly, iAM samples had a higher proportion of subclonal mutations than AMis samples (Figure 2E), suggesting that a high level of ITH was associated with invasiveness. No association between tumor purity and subclonal mutations was observed, showing that our clonality analysis was not confounded by tumor purity (Figure S2F). Since genomic instability is a major source of ITH,[26] we next quantified the level of genomic instability with three independent indices, including weighted genome integrity index (wGII) score, chromosomal copy number heterogeneity score (CNH-DNA), and chromosomal instability score (CIN-RNA).[27–29] As expected, iAM showed a significantly higher level of genomic instability than AMis (Figures 2F and S2G; Table S2). These results indicate that high genomic instability might accelerate tumorigenesis and contribute to acquiring one of the invasion-preferred drivers for AMis.

Transcriptomic comparison of AMis and iAM revealed enrichment of extracellular matrix (ECM) organization, EMT, *KRAS* signaling, macrophage migration, and interferon-γ (IFNγ) response pathways in iAM (Figures S2H–S2J), implying dysregulation of the TME during AM invasion. Altogether, driver mutations, genomic instability, and TME alterations collectively contribute to AM invasion.

Adnexal involvement is associated with a high invasive potential of AMis

To explore clinical predictors for AMis with high invasive potential, we traversed all available clinical variables (Table S1).

(D) Tumor mutational burden, TMB, across melanoma cohorts. CM, cutaneous melanoma; UM, uveal melanoma. The centerline shows the median; boxes indicate the first and third quartiles; whiskers extend 1.5 times the interquartile range. Mann-Whitney U test.
(E) Frequency of alterations across melanoma cohorts. Amp, amplification; Del, deletion; SNV, single nucleotide variant. ***p < 0.001. See also Figure S1, Tables S1 and S2.

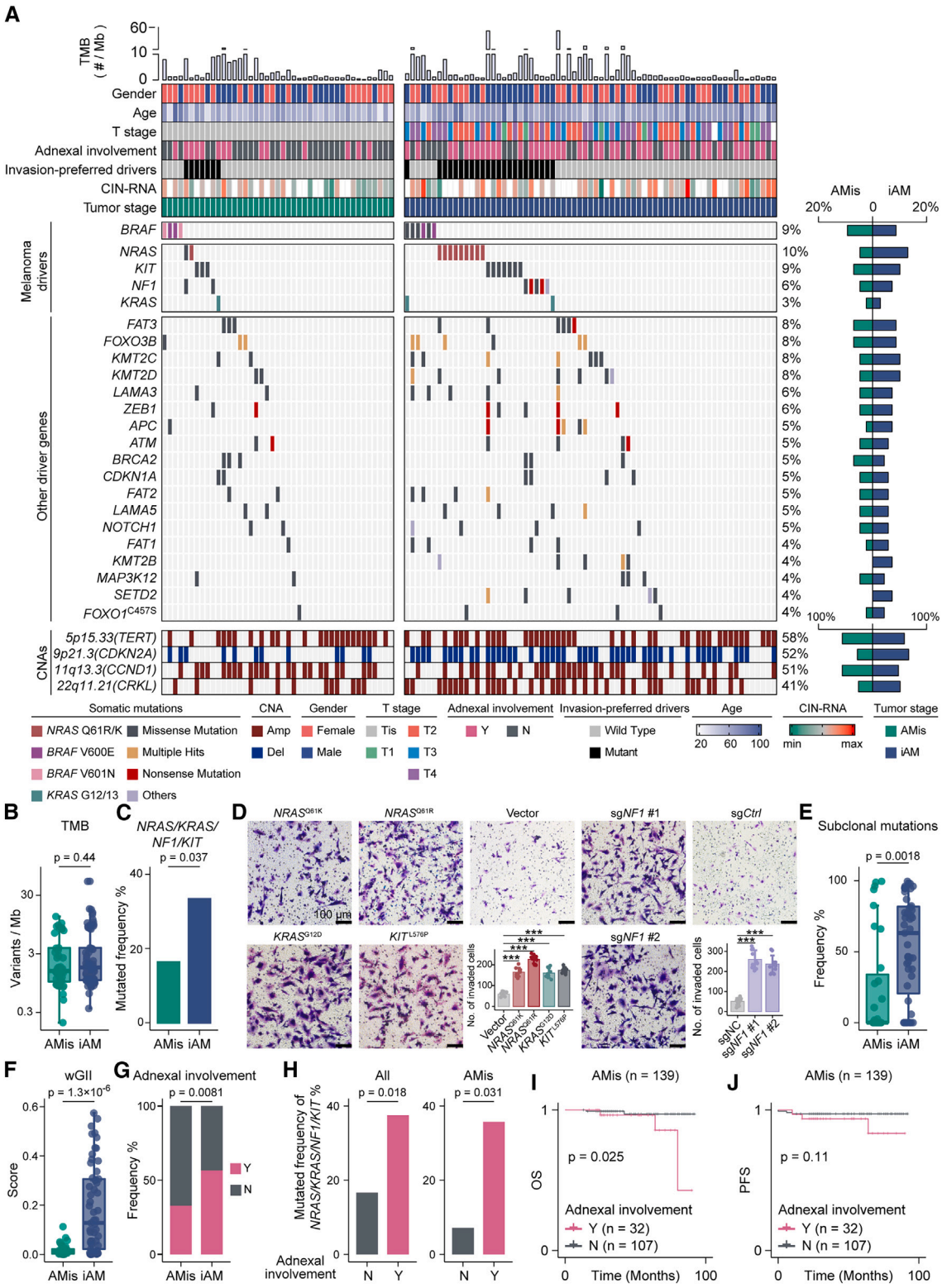

Figure 2. Genomic comparison between AMis and iAM

(A) Landscape of somatic alterations. Tumor mutational burden, TMB, is shown on the top, and altered frequency of each event is shown on the right side as percentages. Amp, amplification; Del, deletion.

(B and C) Comparison of TMB (B, Mann-Whitney U test) and invasion-preferred drivers (C, one-sided Fisher's exact test).

(D) Transwell invasion assays of LM-MEL-45 AM cell lines with driver gene induction or knock-out. Scale bar, 100 μm. Mean ± SD, Student's t test, ***$p < 0.001$.

(legend continued on next page)

Intriguingly, adnexal involvement of AM, defined as the existence of malignant melanocytes in eccrine ducts,[30] was the only variable significantly enriched in iAM compared with AMis (p = 0.0081; Figure 2G). While TMB was comparable (Figure S2K), the mutational frequency of the invasion-preferred drivers was significantly higher in AM with adnexal involvement for either all patients or AMis patients (Figure 2H). In addition, AMis with adnexal involvement had a significantly higher rate of clonal mutations than others (Figures S2L and S2M), suggesting a more homogeneous clonal composition. Adnexal involvement was also associated with higher phosphorylation levels of extracellular signal-regulated kinase (ERK) and AKT (also known as PKB, protein kinase B) in AMis patients (Figures S2N and S2O). These results imply that AMis tumor cells acquiring invasive driver mutations might have a higher proliferation advantage and be subjected to positive selection and clonal expansion (CE). Focusing on patients with AMis, adnexal involvement might serve as a pathological predictor to discriminate AMis tumors with invasive potential from those indolent ones. Supporting this, retrospective analysis of 139 patients with AMis showed that adnexal involvement was linked with shortened overall survival (OS) (p = 0.025; Figure 2I) and progression-free survival (PFS) (p = 0.11, positive trend; Figure 2J) of AMis.

Synchronous AMis-iAM reveals an early and monoclonal seeding pattern for the vertical invasion

To investigate the intra-patient evolutionary dynamics of vertical invasion and regional expansion, we analyzed synchronous AMis-iAM by LCM (Figure 3A). We first compared the genomic landscape across three different types of lesions, including pure AMis, Syn_AMis, and Syn_iAM (Figure 1B). Surprisingly, among 5 patients exhibiting the invasion-preferred drivers, the mutations were shared by paired Syn-AMis and Syn-iAM, but none was detected in pure AMis (Figure 3B). This result suggests that the invasion-preferred driver is acquired before vertical invasion, further corroborating their driver role in AM invasion. Compared with other lesions, Syn_iAM showed a significantly higher percentage of subclonal mutations yet comparable TMB, resulting in higher ITH (Figures 3C and 3D). Consistently, we also observed a significantly higher level of genomic instability in Syn_iAM lesions, as shown by elevated wGII and CNH-DNA scores (Figures 3E and 3F). These results support our aforementioned observation that genomic instability and ITH contribute to AM invasion.

Phylogenetic analysis of matched samples from the same patient revealed a universal pattern of short trunks and long branches, suggesting a high extent of ITH in AM. The percentage of shared mutations, represented by the length of the trunk, in AM was significantly lower than that of CM (p = 0.00057; Figures 3G, 3H, S3A, and S3B).[31] This result indicates a relatively early genetic divergence of Syn_iAM from Syn_AMis, in agreement with its poorer prognosis than CM. Such ubiquitous early seeding patterns were also different from the variable tree structures in other cancers,[26,32,33] suggesting a unique invasion process of AM.

We next inferred the origin and timing of vertical invasion. Jaccard similarity index (JSI) can distinguish monoclonal seeding (JSI $<$ 0.3) from polyclonal seeding (JSI $\geq$ 0.3).[34] We observed a ubiquitous monoclonal seeding pattern for all patients (Figure 3I; Table S3). In agreement with this, mutations of the invasion-preferred drivers were mostly clonal in both Syn_AMis and Syn_iAM (Figure 3J). Patients with multiple Syn_AMis lesions could provide more insights on the genetic relationship between Syn_AMis and Syn_iAM (Figure 3K). In patient AM18, phylogenetic analysis showed that Syn_iAM originated from the adjacent Syn_AMis_2 rather than the distant Syn_AMis_1. Of note, the $NRAS^{Q61K}$ mutation was among a few mutations shared by Syn_AMis_2 and Syn_iAM yet absent in Syn_AMis_1. This result indicates that Syn_AMis invaded the dermal layer soon after acquiring $NRAS^{Q61K}$, supporting its role to drive vertical invasion. Similar mutation spectrums of the non-shared mutations across the three regions suggested a shared mutagenic background (Figures 3K and S3A). Additionally, two patients with paired primary tumor and metachronous relapse/metastasis showed an early divergence near the root of the tree, indicating that relapse/metastasis occurred early (Figures S3C and S3D). These results emphasize the high degree of ITH in AM and the necessity of early detection.

Two evolutionary patterns of the regional expansion

To interrogate the evolutionary patterns of regional expansion, we inferred the clonal composition via cancer cell fraction (CCF) analysis (Figure 3L). Pairwise CCF distribution showed that 81.8% (9/11) of Syn_AMis lesions exhibited a clonal peak, in sharp contrast to the 44.4% (4/9) of Syn_iAM lesions (Figures 3M and S3E). Therefore, Syn_AMis tended to exhibit a more homogeneous composition, consistent with our aforementioned observation that AMis with adnexal involvement, i.e., high invasive potential, exhibited more clonal mutations. In Syn_iAM, we characterized two distinct evolutionary patterns of regional expansion: (1) CE, in which invasive tumors remain clonal and (2) subclonal diversification (SD), in which tumors acquire diverse subclones (Figure 3L). Patients stratified into the SD pattern exhibited a higher degree of ITH that was not confounded by tumor purity (Figures 3N and 3O). Considering that high ITH could generate subclonal drivers,[26,35] we speculated that the SD process facilitated the acquisition of drivers that boost the regional expansion (Figure 3P).

Integrative analysis identifies three molecular subtypes

Unsupervised hierarchal clustering of 81 AM samples with bulk RNA-seq data identified three distinct molecular subtypes, named as C1, C2, and C3 (Figure 4A; Table S4). Subtype C1 showed elevated keratin genes (Figure S4A), skin development and

(E and F) Comparison of subclonal mutations (E) and wGII score (F). Mann-Whitney U test.
(G) Frequency of patients with (Y) or without (N) adnexal involvement. Fisher's exact test.
(H) Mutated frequency of invasion-preferred drivers with or without adnexal involvement among all patients (left) and AMis patients (right). Fisher's exact test.
(I and J) Overall survival, OS, (I) and progression-free survival, PFS, (J) of AMis stratified by adnexal involvement status. Log-rank test. Data are represented as boxplots in (B, E, and F). The centerline shows the median; boxes indicate the first and third quartiles; whiskers extend 1.5 times the interquartile range. See also Figure S2 and Table S2.

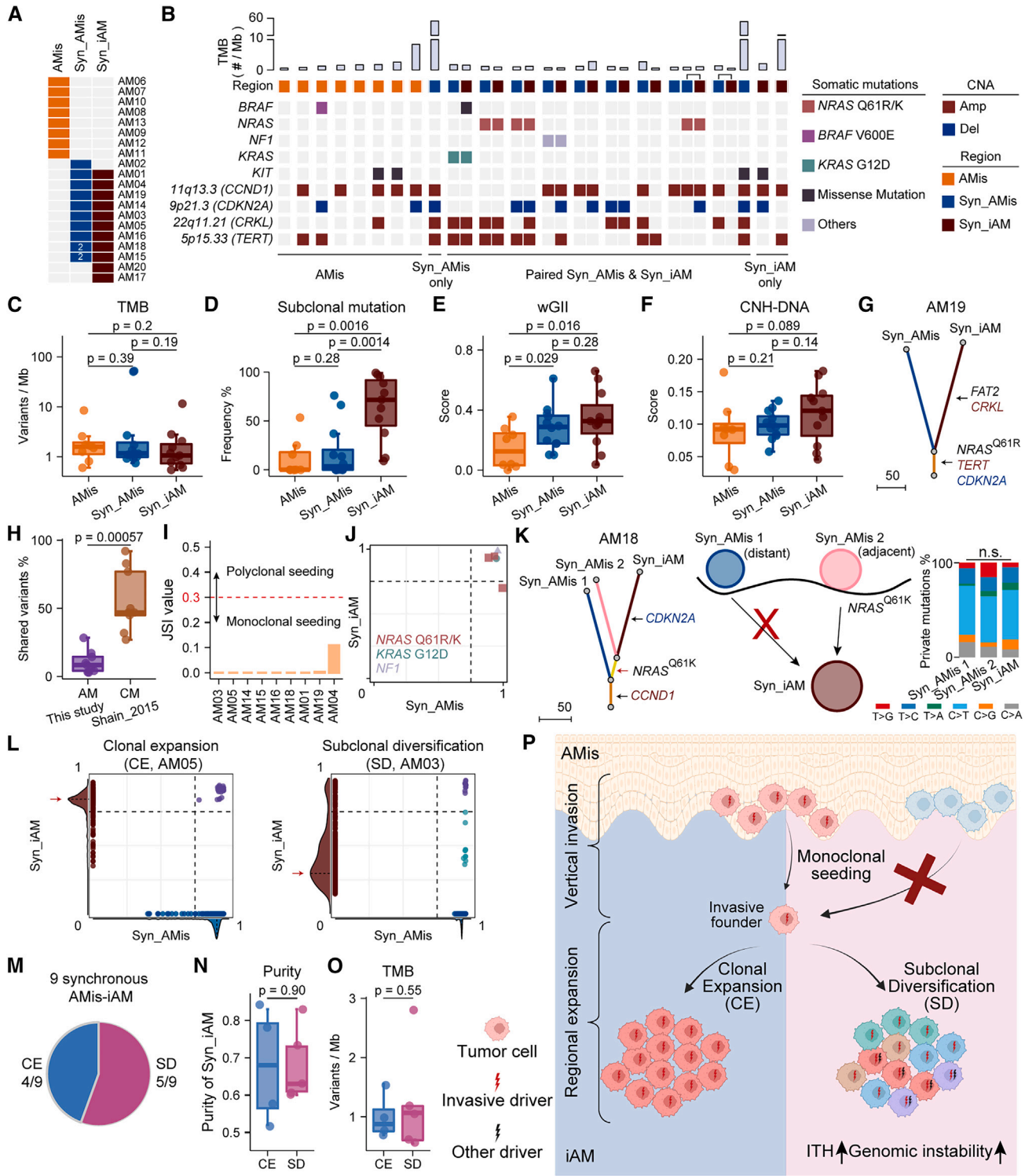

Figure 3. Evolutionary dynamics of AM invasion

(A and B) Sampling information (A) and mutational landscape (B) of laser-capture microdissection, LCM, regions. Matched regions are arranged together. Amp, amplification; Del, deletion.

(C–F) Boxplots comparing tumor mutational burden, TMB (C), subclonal mutations (D), wGII (E), and CNH-DNA (F) scores. One-sided Mann-Whitney U test.

(G) Phylogenetic tree of AM19. Black, mutation; red, copy number gain; blue, copy number loss. Scale bar, 50 mutations.

(H) Comparison of shared variants. Mann-Whitney U test.

(I) Jaccard similarity index (JSI) of patients with two or more regions. Dashed line indicates the threshold of 0.3.

(legend continued on next page)

keratinization pathways (Figure 4B), and low mitogen-activated protein kinase (MAPK) activity (Figure S4B), thus was denoted as the "keratin" subtype. Subtype C2 showed upregulation of chromatin remodeling genes (*KMT2A* and *KMT2C*), DNA and histone methylation pathways, suggesting a "chromatin remodeling" phenotype. Subtype C3 exhibited upregulation of EMT-related genes (*TWIST2* and *VIM*), ECM organization and macrophage infiltration pathways, and high proliferation activity, together proposing a "proliferation" phenotype (Figures 4A, 4B, S4A, and S4B).

Comparable TMB indicated that our classification was not subjected to sampling biases (Figure S4C). Subtype C3 exhibited the highest CIN-RNA, wGII, and CNH-DNA scores, indicating high genomic instability (Figure 4C). Consistently, the C3 subtype showed the highest proportion of subclonal mutations (Figure 4D). These results collectively explain the malignant characteristics of the C3 subtype from a genomic perspective. As expected, the three subtypes showed distinct PFS and OS, with C3 subtype exhibiting the poorest prognosis (Figures 4E and S4D). This result showed that our classification was robust and clinically relevant.

In contrast to C1 and C2, which were an even mixture of AMis and iAM, subtype C3 was highly enriched with iAM (27/28) (Figure 4A), indicating a unique subset of iAM. Compared with iAM in C1 and C2 (referred to as non-C3 iAM hereafter), C3 iAM exhibited a shortened PFS (Figure 4F) and distinct malignant phenotypes (Figures S4E–S4L). Importantly, C3 iAM exhibited significantly more subclonal mutations (Figure 4G). 81% of C3 iAM corresponded to the SD pattern in contrast to the 44% of non-C3 iAM (Figure 4H). This result partially explained the dismal prognosis of C3 iAM. Of note, no significant differences in the tumor T stage, as determined by Breslow thickness and ulceration, were found between the two groups (Figures 4I, S4M, and S4N), suggesting that the invasion depth of AM may not necessarily correlate with its progression ability. Multivariate analysis confirmed that our AM subtyping is an independent prognostic factor (Figures 4I and S4M). The observation that classification of C3 iAM is independent to the tumor stages could be validated by a published dataset (Figures S4O and S4P).[6] Our subtyping highlighted that early-stage tumors (T1 and T2) in the C3 subtype may exhibit highly malignant behavior and progress rapidly. Therefore, biomarkers are needed for the early detection of these C3 tumors, especially when the tumors are relatively small in size.

Three molecular subtypes exhibit distinct TME composition

Consensus TME phenotypes were observed for the three molecular subtypes (Figures 4J and S5A; Table S4). Subtype C1 showed the lowest level of immune infiltration and pro-tumor cytokines, and was designated "Low-immune". Subtype C2 showed the highest abundance of B cells and a relatively higher T cell cytotoxicity, and designated as "Immune Activated". Subtype C3 showed the highest levels of immune infiltration, tumor-associated macrophages (TAMs), and EMT (Figures S5B–S5D). TAMs in C3 were mainly immunosuppressive macrophages (Figure 4K), showing high expression of *CD163*, *APOE*, *C1QC* (Figure 4L),[36] and therapeutic targets like *VSIG4* and *CSF1R* (Figure S5B). These results together proposed an "Immune Suppressed" phenotype for C3.

Consistent with the comparable TMB across the three subtypes, TMB was not correlated with the TAM score (Figure S5E). By contrast, the TAM score correlated with genomic instability indices, including wGII (Figure 4M) and CNH-DNA scores (Figure S5F), and subclonal mutations (Figure 4N). In addition, TAM score correlated with the EMT score (Figures 4O and S5G) and poor prognosis in our cohort (Figures 4P, 4Q, and S5H). These results collectively indicate that TAM infiltration might promote tumor EMT and genomic instability for the C3 subtype and lead to poor prognosis.

scRNA-seq reveals APOE$^+$/CD163$^+$ macrophage subsets

To interrogate the tumor and TME heterogeneity at the single-cell level, we performed scRNA-seq on 8 AMis and 16 iAM tumors. A total of 223,023 cells were harvested after stringent quality control and divided into 13 major cell populations (Figures 5A and S6A–S6D; Table S5). Pseudo-bulk analysis with signature genes for each subtype successfully identified all three subtypes (Figure 5B). Malignant cells (Figure S6E) could be divided into 8 cell states, including melanocytic, EMT, IFN response, antigen presentation, cycling, RNA processing, and two stress-related states (Figures 5C and 5D). These states of AM cells were generally consistent with previously reported cell states of CM (Figure S6F).[37–39] Consistent with our findings on the bulk level, tumor cells in C3 subtypes exhibited the highest EMT score (Figure 5E).

Five subsets of macrophages were identified, including Mph_APOE_CD163, Mph_APOE, Mph_CD163, Mph_ISG15, and Mph_TIMP1 (Figures 5F and S6G). Polarization analysis showed that Mph_APOE_CD163, Mph_CD163, and Mph_APOE were all immunosuppressive TAMs, hence collectively named APOE$^+$/CD163$^+$ TAMs (Figure S6H). APOE$^+$/CD163$^+$ TAMs were significantly enriched in the C3 subtype (Figure 5G) and positively correlated with EMT scores (Figure 5H), validating our observations on the bulk level. Ligand-receptor analysis showed that macrophages exhibited the most abundant cell-cell interactions. High levels of self-recruitment and interactions were observed within APOE$^+$/CD163$^+$ macrophages (Figures 5I and S6I). APOE$^+$/CD163$^+$ macrophages might promote the phenotypic transition of tumor cells through EMT-related signaling pathways, including

(J) Cancer cell fraction (CCF) plot of invasion-preferred drivers.
(K) Phylogenetic tree (left), schematic (middle), and mutational spectrum (right) of AM18. Chi-square test.
(L) Representative CCF plots of clonal expansion (CE) and subclonal diversification (SD). Mutations are divided into four groups: private in Syn_AMis (blue), private in Syn_iAM (red), clonal in both regions (CCF $\geq$ 0.75, purple), and others (green). Kernel density of mutations is also shown, with the peak denoted by red arrows.
(M) Pie chart showing proportions of CE and SD.
(N and O) Comparison of tumor purity (N) and TMB (O). Mann-Whitney U test.
(P) Schematic of clonal dynamics during AM invasion. Data are represented as boxplots in (C–F, H, N, and O). The centerline shows the median; boxes indicate the first and third quartiles; whiskers extend 1.5 times the interquartile range. See also Figure S3 and Table S3.

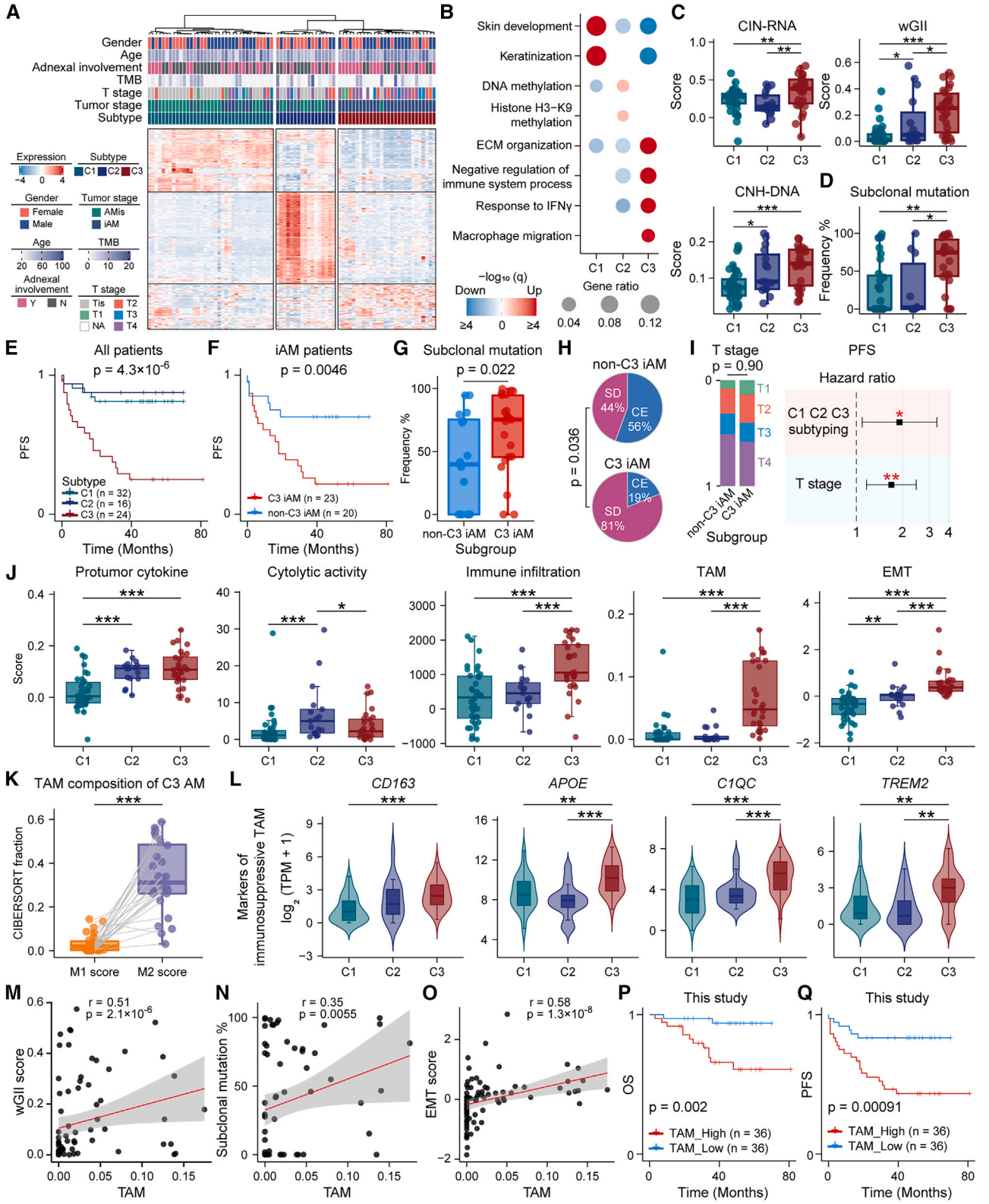

(legend on next page)

TGFB1-TGFBR2, *TNF-TNFRSF1B*, and *IGF1-IGF1R* (Figure 5J).[40,41] Multi-color immunohistochemistry (mIHC) validated the existence of APOE$^+$ macrophages (Mph_APOE), CD163$^+$ macrophages (Mph_CD163), and double-positive macrophages (Mph_APOE_CD163) (Figure 5K). Additionally, APOE$^+$/CD163$^+$ TAMs, as well as its positive correlation with tumor EMT scores, were validated using publically available AM scRNA-seq datasets (Figures S6J–S6N).[22,23]

Spatial transcriptomic analysis confirms the direct contact and close interaction between APOE$^+$/CD163$^+$ TAMs and EMT tumor cells

To investigate whether APOE$^+$/CD163$^+$ TAMs interact with EMT^{high} tumor cells on the spatial level, we performed spatial transcriptomics (ST) in 10 AM samples. Structures of multiple epidermal layers, including basal, spinosum, and granulosum, as well as the subcutaneous structure of eccrine sweat gland and blood vessels can be clearly visualized, demonstrating the high quality of our ST data (Figure 6A). Tumor regions can be identified by the high expression of melanoma signature genes like *MLANA*, *PMEL*, *TYPR*, and *DCT* (Figure 6B). For example, in a C3 iAM patient, AM140, the tumor region is composed of EMT^{high} tumor cells, characterized by elevated expression of *CDH2*, and highly infiltrated with APOE$^+$/CD163$^+$ TAMs. By contrast, such co-existence could not be identified in the non-C3 patients, AM147.

We next performed quantitative analysis based on Voronoi diagrams after single cell segmentation. Cell identities were assigned by integrating ST data with scRNA-seq using CytoSPACE.[42] Cells mapped to the single cell-based tumor EMT state were defined as EMT tumor cells, while non-EMT tumor cells were those mapped to other tumor states (Figures 6C and S7A). As expected, C3 patients showed a significantly higher proportion of EMT tumor cells, as well as a significantly higher level of APOE$^+$/CD163$^+$ macrophage infiltration (Figure 6D). Among C3 patients, APOE$^+$/CD163$^+$ macrophages located much closer to EMT tumor cells compared with non-EMT cells (Figure 6E). CellChat analysis showed that APOE$^+$/CD163$^+$ macrophage exhibited high activities as both the sender (ligand) and receiver (receptor), confirming the high level of cell-cell interactions (Figure 6F).[43] Our previous single cell analysis showed that *IGF1-IGF1R* might mediate the interaction between APOE$^+$/CD163$^+$ macrophages and EMT tumor cells. Consistent with this finding, APOE$^+$/CD163$^+$ macrophages exhibited the highest level of insulin growth factor (IGF) signaling network as sender and influencer cells, compared with other immune cells (Figure 6G). These spatial data revealed the direct contact and close interaction between APOE$^+$/CD163$^+$ TAMs and EMT tumor cells.

Multiplexed spatial proteomics validates the interaction between APOE$^+$/CD163$^+$ TAMs and EMT tumor cells

To further validate the spatial distribution and interaction between APOE$^+$/CD163$^+$ TAMs and EMT tumor cells at the protein level, we performed 22-plex CODEX in 12 AM samples (Figures 7A and S7B; Table S6). Epidermis was marked by pan-cytokeratin (pan-CK) and E-cadherin. Tumor cells were identified by positive expression of Melan-A. Immune cell infiltration was also observed in the tumor region, including CD4$^+$ T cells (CD3e and CD4), CD8$^+$ T cells (CD3e and CD8), B cells (CD20), macrophages (CD68), and dendritic cells (CD11c). In the adjacent normal region, the eccrine sweat gland was marked by pan-CK expression and the ductal structure. Adnexal involvement could be clearly identified by tumor cells directly contacting the eccrine sweat gland.

EMT tumor regions could be identified in the C3 patients while the non-C3 patients were mainly composed of non-EMT tumor regions (Figure 7B). Spatial mapping revealed a positive correlation between APOE$^+$/CD163$^+$ TAMs and EMT tumor cells (Figure 7C). Significantly higher expression levels of both IGF1 and IGF1R were observed in the C3 patients (Figure 7D). Interestingly, a C3 patient, AM138, contained both EMT^{high} and EMT^{low} regions, enabling the intra-patient comparison (Figure 7E). APOE$^+$/CD163$^+$ TAMs were highly accumulated in the EMT^{high} region (Figure 7F). The expression of both IGF1 and IGF1R were also significantly elevated in the EMT^{high} region (Figure 7G). These results validated our observations at both single cell and ST level, supporting that APOE$^+$/CD163$^+$ TAM might promote the EMT of tumor cells via IGF1-IGF1R interaction.

Ex vivo and *in vitro* assays show that APOE$^+$CD163$^+$ TAMs promote tumor EMT via IGF1-IGF1R interaction

We next performed functional assays to interrogate the interplay between APOE$^+$/CD163$^+$ macrophages and EMT tumor cells.

Figure 4. Molecular subtypes and TME of AM

(A) Three molecular subtypes inferred from bulk RNA-seq data. Clinical and genomic characteristics are annotated.

(B) Gene Ontology (GO) analysis. Gene ratio, percentage of specific pathway genes presented in differentially expressed genes; q, Benjamini-Hochberg adjusted *p* value.

(C and D) Comparison of CIN-RNA, wGII, and CNH-DNA scores (C), and subclonal mutations (D).

(E and F) Progression-free survival, PFS, of all patients (E) and iAM patients (F) based on molecular subtypes.

(G) Comparison of subclonal mutations.

(H) Proportion of iAM patients assigned to subclonal diversification, SD, or clonal expansion, CE.

(I) T stage distribution (left) and multivariate Cox regression analysis of PFS (right) based on subtyping.

(J) Comparison of tumor microenvironment, TME, signatures. TAM, tumor-associated macrophage; EMT, epithelial-mesenchymal transition.

(K) TAM composition of C3 AM.

(L) Expression of immunosuppressive TAM markers.

(M–O) Correlation between TAM and subclonal mutations (M), wGII (N), or EMT (O) scores.

(P and Q) Overall survival, OS (P) and PFS (Q) of AM patients stratified by TAM score. Data are represented as boxplots in (C, D, G, and J–L). The centerline shows the median; boxes indicate the first and third quartiles; whiskers extend 1.5 times the interquartile range. Statistical differences determined with Mann-Whitney U test in (C, D, and J–L), one-sided Mann-Whitney U test in (G), Fisher's exact test in (H), Spearman correlation test (M–O), and log-rank test in (E, F, P, and Q). $^*p < 0.05$, $^{**}p < 0.01$, $^{***}p < 0.001$. See also Figures S4 and S5, and Table S4.

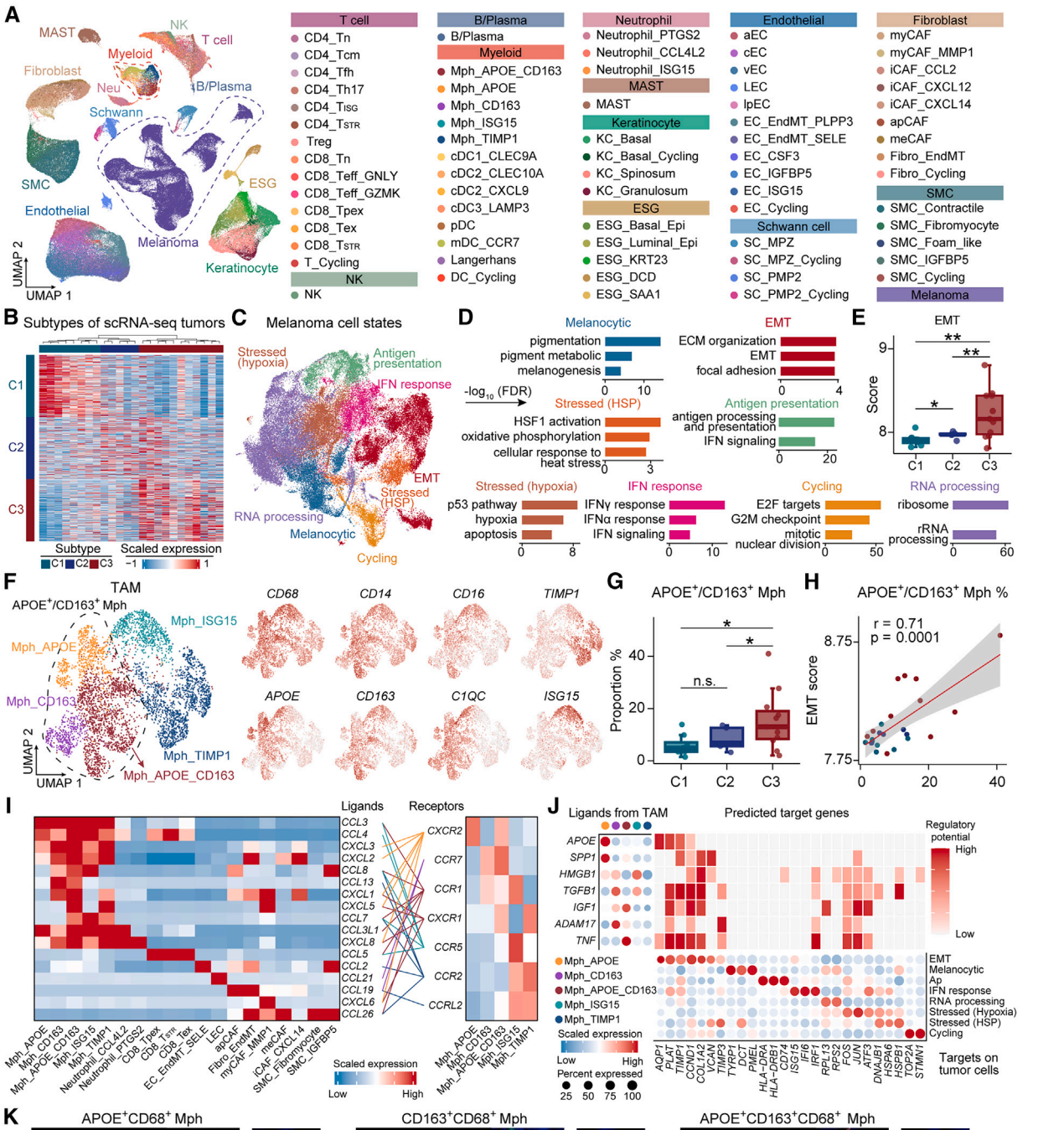

(legend on next page)

Ex vivo analysis of macrophages isolated from paired peripheral blood and tumor tissues showed that APOE$^+$CD163$^+$ macrophages were significantly enriched in the tumor tissue (Figure 8A). To investigate whether AM tumor cells could directly induce the APOE$^+$CD163$^+$ phenotype of macrophages, we isolated monocytes from healthy donors and co-cultured them with the conditioned medium (C.M.) from the LM-MEL-45 cell line *in vitro*. Flow cytometry analysis showed that the proportion of APOE$^+$CD163$^+$ macrophages gradually increased from 1.2% at day 0 to 73.5% at day 14 (Figures 8B and S8A). RNA-seq analysis also validated the time-dependent induction of APOE$^+$CD163$^+$ macrophages, as demonstrated by the continuously elevated expression of marker genes like *APOE*, *CD163*, *C1Q*, and *IGF1* (Figure 8C). Gene Set Enrichment Analysis (GSEA) analysis showed the enrichment of APOE$^+$CD163$^+$ signature in the macrophages at day 14, compared with the control group (Figure 8D). Such elevated expression of *APOE* and *CD163* in macrophages could also be detected at the protein level (Figure 8E). These results showed that AM cells could induce the APOE$^+$CD163$^+$ phenotype of macrophages.

We next explored whether APOE$^+$CD163$^+$ macrophages could promote the EMT of tumor cells. *Ex vivo* analysis confirmed that C3 patients exhibited a significantly higher proportion of EMT tumor cells than that of non-C3 patients (Figure 8F). After coculturing with APOE$^+$CD163$^+$ macrophages *in vitro*, the LM-MEL-45 tumor cells expressed significantly higher levels of mesenchymal marker genes, including *CDH2*, *TWIST1/2*, *SNAI1/2*, etc. (Figure 8G). An elevated EMT signature was also enriched in the cocultured tumor cells, compared with tumor cells alone (Figure 8H). Supporting this phenotype, tumor cells changed from a rounded shape to an elongated one after 5 days of coculture. To explore the secretion of IGF1 from APOE$^+$CD163$^+$ macrophages (Figure 8I), ELISA analysis showed that the secreted IGF1 protein in the lower chamber continuously elevated after cocultured with APOE$^+$CD163$^+$ macrophages (Figure 8J). Importantly, inhibition of this interaction by the IGF1 inhibitor xentuzumab, the IGF1R inhibitor linsitinib, or knocking-out *IGF1R* in tumor cells could significantly reduce the N-cadherin expression, and reverse tumor cells back to the round shape and the re-expression of E-cadherin (Figures 8K and 8L). Taken together, these results demonstrated that APOE$^+$CD163$^+$ macrophages could promote the EMT of tumor cells via IGF1-IGF1R interaction.

APOE$^+$CD163$^+$ staining is a biomarker for inferior AM prognosis

The aforementioned results intrigued us to further interrogate the prognostic value of CD163 and APOE expression for AM patients. On the bulk RNA level, both *APOE* and *CD163* expression were significantly correlated with the TAM score (Figures S8B and S8C), and the combination of *APOE* and *CD163* showed the highest prediction power for the C3 subtype (Figure S8D) and post-surgery progression (Figure S8E). On the protein level, we performed IHC staining on 96 AM patients with tissue sections available in the discovery cohort (Figures 8M and S8F; Table S7). Notably, patients with APOE$^+$CD163$^+$ macrophages had a five-year PFS of 54.7%, much worse than the 90.5% for those patients without APOE$^+$CD163$^+$ macrophages (p = 0.00017; Figure 8N). We also performed IHC staining on 87 AM patients in an independent validation cohort. Consistently, double-positive staining of APOE and CD163 was significantly associated with shortened PFS (p = 0.0019) and OS (p = 0.0051) of AM patients (Figure 8O). Such double-positive signals were also associated with poor prognosis in a published AM dataset (Figure S8G). In addition, iAM and C3 patients showed significant enrichment of APOE$^+$CD163$^+$ than their counterparts, and the double-positive staining of these two markers was an independent predictor (Figures S8H–S8K). Taken together, these results showed that APOE and CD163 staining could serve as a promising prognostic biomarker for patients with AM.

DISCUSSION

Early diagnosis and prevention can significantly improve patient survival in most cancer types.[15] Our identification of adnexal involvement correlated with high invasive ability of AMis showed promising clinical value. First, AMis lesions exhibit distinct invasive abilities, consistent with the clinical observation that some AMis quickly progress and invade the dermis while others may remain in the epidermis for years.[13] Second, AMis with higher invasive potential can be efficiently distinguished from indolent AMis by routine pathological examination or genetic screening. Detailed pathological examination of the dermis should be performed on these AMis with adnexal involvement to avoid missing detection of invasive tumor cells. By contrast, those indolent pure AMis are potential precursor lesions that do not have the

Figure 5. TME of AM at the single-cell resolution

(A) Cell annotation. ESG, eccrine sweat gland; Neu, neutrophil; SMC, smooth muscle cell. See full abbreviation list in Table S5.

(B) Subtyping of 24 tumors based on scRNA-seq. Rows denote the top 200 significantly upregulated genes in each subtype; columns indicate individual samples.

(C) Cell states of tumor cells.

(D) Enriched functional terms for each cell state.

(E) Epithelial-mesenchymal transition, EMT, scores among three subtypes. One-sided Student's t test.

(F) Tumor-associated macrophages, TAMs, labeled by cluster identities (left) and marker gene expressions (right).

(G) Comparison of APOE$^+$/CD163$^+$ macrophage proportions. One-sided Student's t test.

(H) Sperman correlation between APOE$^+$/CD163$^+$ macrophage proportions and EMT scores across patients. Points colored by molecular subtypes.

(I) Ligand-receptor analysis based on CellPhoneDB. Scaled expression heatmap of chemokine genes among cell clusters (left) and TAM clusters (right). Interactions are connected by lines and colored by the dominant TAM clusters.

(J) Ligand-receptor analysis based on NicheNet. Dot plots show predicted top ligands in TAM (left) and targets in tumor cells (bottom), and the heatmap shows interaction potential (middle). Ap, antigen presentation.

(K) Representative mIHC images showing APOE$^+$ (left), CD163$^+$ (middle), and APOE$^+$CD163$^+$ macrophages (right). Scale bar, 10 μm. Data are represented as boxplots in (E and G). The centerline shows the median; boxes indicate the first and third quartiles; whiskers extend 1.5 times the interquartile range. $^*p < 0.05$, $^{**}p < 0.01$. See also Figure S6 and Table S5.

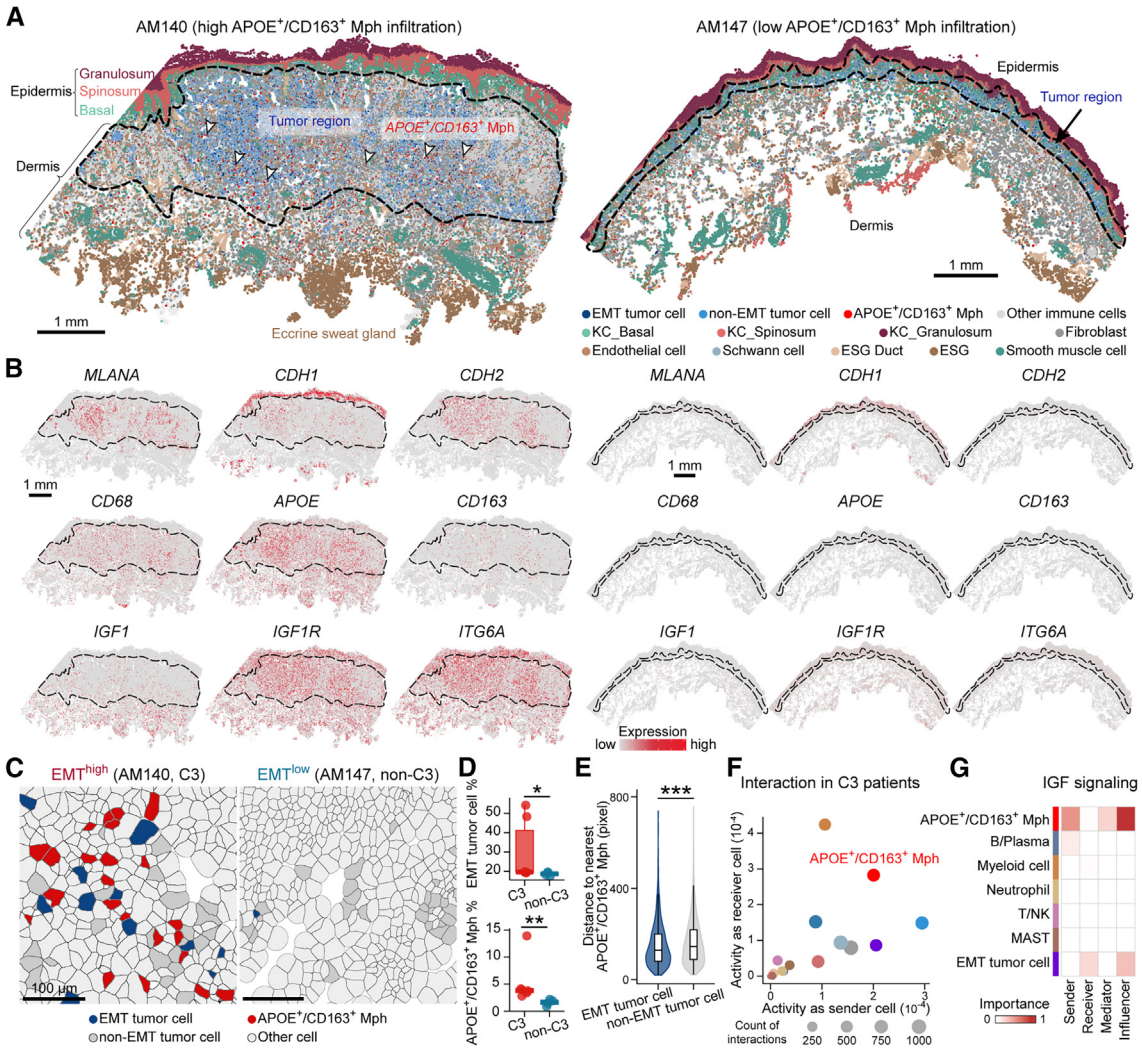

Figure 6. Spatial transcriptomics analysis

(A) Annotated spatial map of AM140 and AM147. Black dashed lines denote tumor regions. Scale bar, 1 mm.

(B) Spatial expression levels of selected marker genes. Scale bar, 1 mm.

(C) Representative images of single cell segmentation. Scale bar, 100 μm.

(D) Proportions of epithelial-mesenchymal transition, EMT, tumor cells (top) and APOE$^+$/CD163$^+$ macrophages (bottom) between C3 and non-C3 tumors. One-sided Mann-Whitney U test. *$p < 0.05$, **$p < 0.01$.

(E) Comparison of the distance of tumor cells to the nearest APOE$^+$/CD163$^+$ macrophage in C3 patients. Student's t test. ***$p < 0.001$.

(F) Activities of cells acting as sender cells (x axis) or receiver cells (y axis) in C3 patients based on CellChat.

(G) IGF signaling interactions across cell clusters. Data are represented as boxplots in (D and E). The centerline shows the median; boxes indicate the first and third quartiles; whiskers extend 1.5 times the interquartile range. See also Figure S7.

capacity to progress, which may lead to overdiagnosis. Further investigations are warranted to identify biomarkers for these indolent AMis. Third, we recommend regular follow-up checks for these patients with high-invasion AMis after surgical resection to monitor disease progression.

The evolutionary dynamics of melanoma have been intensively investigated, while those of AM remained unclear.[44,45] AM exhibits a prominent field effect. Certain genetic and environmental factors lead to multiple nests of transformed cells or precursor lesions in the skin. Acral nevi are a special form of precursor lesion in AM. Smalley et al. showed that *BRAF* mutated at a high frequency of 86% in acral nevi, indicating that acral nevi may not be the precursor lesion for most AM.[25] Our identification of *BRAF* mutation not included in the four invasion-preferred drivers is consistent with this observation. Our cohort only involves AMis and iAM yet lacks adjacent normal skin. Detailed genomic profiling of the normal regions may give additional insights into the field effect of AM.

We showed that during vertical invasion, the tumor cells followed an early and monoclonal seeding pattern. The monoclonal seeding pattern suggested that AM invasion followed an evolutionary bottleneck model within which additional mutations of the invasion-preferred drivers were required to facilitate vertical invasion. Therefore, patients with AM may benefit from advances

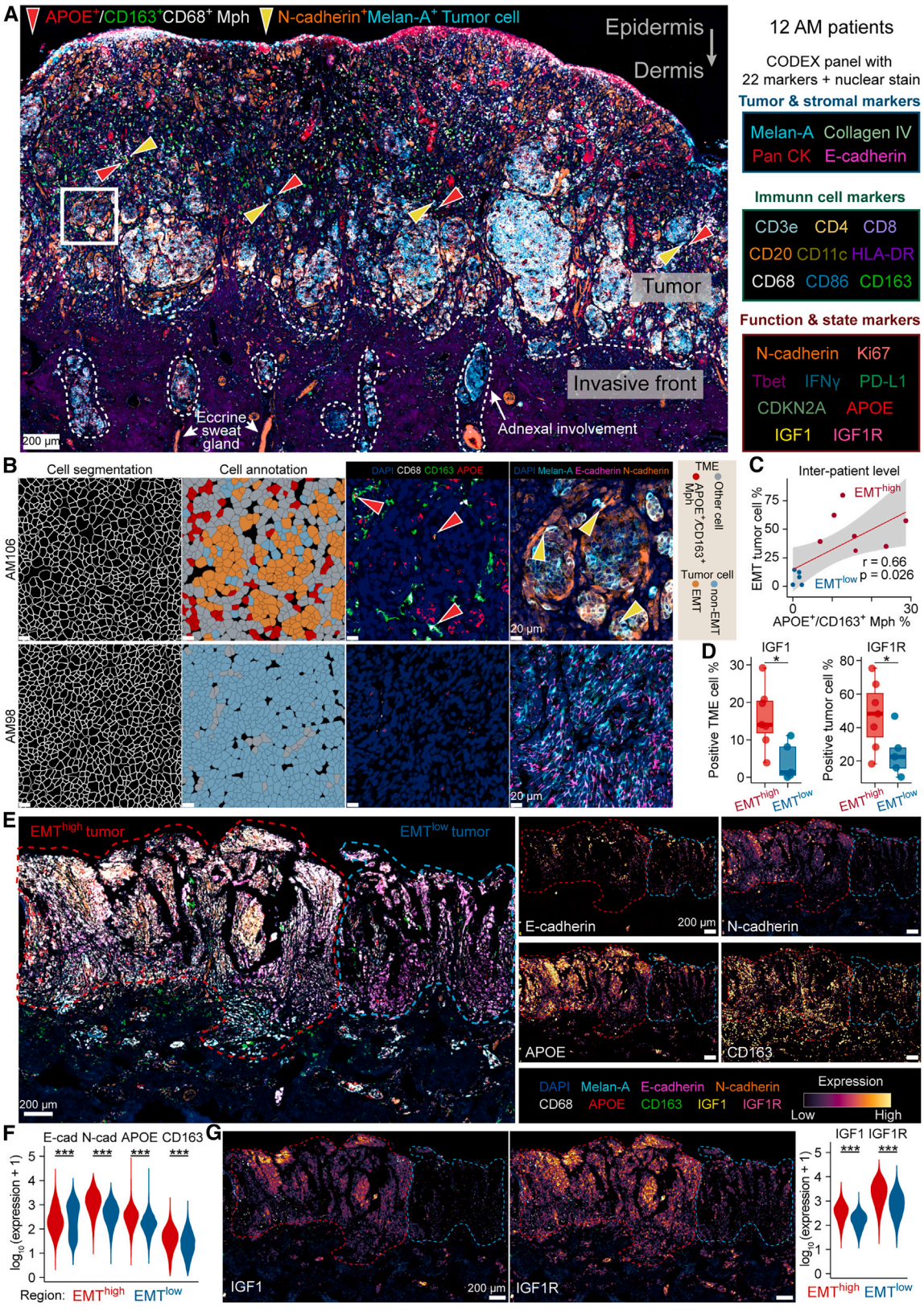

(legend on next page)

in therapies targeting these driver mutations.[46] The early seeding pattern highlighted the necessity of early detection of AMis before invasion. A recent study described the positional oncogenesis for AM,[47] which raises the possibility that iAM directly originates from adnexal structure and there may be a different cell of origin to AMis. However, in our cohort, many identical mutations were shared between matched Syn_AMis and Syn_iAM lesions, suggesting that iAM was derived from AMis rather than from an independent lineage. During regional expansion, the SD process may be driven by a high level of genomic instability. The accumulation of subclonal mutations could propel the acquisition of additional drivers and boost the progression of iAM. Consistent with this finding, close associations among the SD pattern, higher genomic instability, higher ITH, and poor prognosis were identified in the C3 iAM.

Recent single cell analyses characterized lower overall immune infiltration and fewer effector $CD8^+$ T cells and natural killer (NK) cells in AM, depicting a more suppressive immune microenvironment, compared with CM.[22,23] Our integrative analysis highlighted a unique population of immunosuppressive $APOE^+/CD163^+$ macrophages. CD163 has long been used as a pan-macrophage marker and is associated with immunosuppression.[48] APOE is mainly involved in lipoprotein metabolism and widely expressed across tumor and immune cells.[49] $C1Q^+TREM2^+APOE^+$ macrophages are reported to be associated with early recurrence in clear cell renal cell carcinoma.[36] The functional role and clinical relevance of $APOE^+/CD163^+$ macrophages remain less explored. Our study demonstrates that $APOE^+/CD163^+$ macrophages could promote the EMT of tumor cells via the IGF1-IGF1R interaction, thus exhibiting a pro-tumor role and are associated with poor prognosis. APOE and CD163 staining could also serve as efficient biomarkers to identify the C3 iAM or AM patients with a worse prognosis, which might benefit from treatments targeting the IGF1-IGF1R interaction. Of note, 50% of early-stage tumors (T1 and T2 stages) are determined as the C3 iAM. APOE and CD163 staining may also help identify these iAM tumors with high progression capacity at a relatively early timing point. In sum, our study provides clinical implications for the diagnosis, prognosis, and treatment of AM.

STAR★METHODS

Detailed methods are provided in the online version of this paper and include the following:

SUPPLEMENTAL INFORMATION

Supplemental information can be found online at https://doi.org/10.1016/j.ccell.2024.04.012.

ACKNOWLEDGMENTS

This study was supported by the National High Level Hospital Clinical Research Funding (High Quality Clinical Research Project of Peking University First Hospital), the National Key Research and Development Project of China (2022YFC3400900 and 2022YFC2504702), the National Natural Science Foundation of China (82322047, 82173035, 82073015, 82273502, 81988101, 82141103, and 81802813), the Beijing Municipal Natural Science Foundation (7202202), the Beijing Nova Program (20230434854), and the Clinical Medicine

Figure 7. Spatial proteomics analysis

(A) A representative CODEX image. Red arrows, $APOE^+/CD163^+$ macrophages; yellow arrows, epithelial-mesenchymal transition (EMT) tumor cells. Scale bar, 200 μm.

(B) Representative images showing cell segmentation, annotation, $APOE^+/CD163^+$ macrophages (red arrows), and EMT tumor cells (yellow arrows). Scale bar, 20 μm.

(C) Sperman correlation between infiltration of $APOE^+/CD163^+$ macrophages and EMT tumor cells.

(D) Proportions of $IGF1^+$ (left) or $IGF1R^+$ (right) cells. The centerline shows the median; boxes indicate the first and third quartiles; whiskers extend 1.5 times the interquartile range. Student's t test. $^*p < 0.05$.

(E) CODEX images of AM138 (left). Tumor cells ($Melan\text{-}A^+$); EMT^{high} ($E\text{-}cadherin^{low}$, $N\text{-}cadherin^{high}$), EMT^{low} ($E\text{-}cadherin^{high}$, $N\text{-}cadherin^{low}$). Expression levels of individual marker proteins are shown on the right side. EMT^{high} and EMT^{low} regions are marked by dashed lines. Scale bar, 200 μm.

(F) Protein expression levels in segmented cells between EMT^{high} and EMT^{low} regions. Mann-Whitney U test. $^{***}p < 0.001$.

(G) Spatial maps (left) and protein expression levels (right) of IGF1 and IGF1R. Scale bar, 200 μm. Mann-Whitney U test. $^{***}p < 0.001$. See also Figure S7 and Table S6.

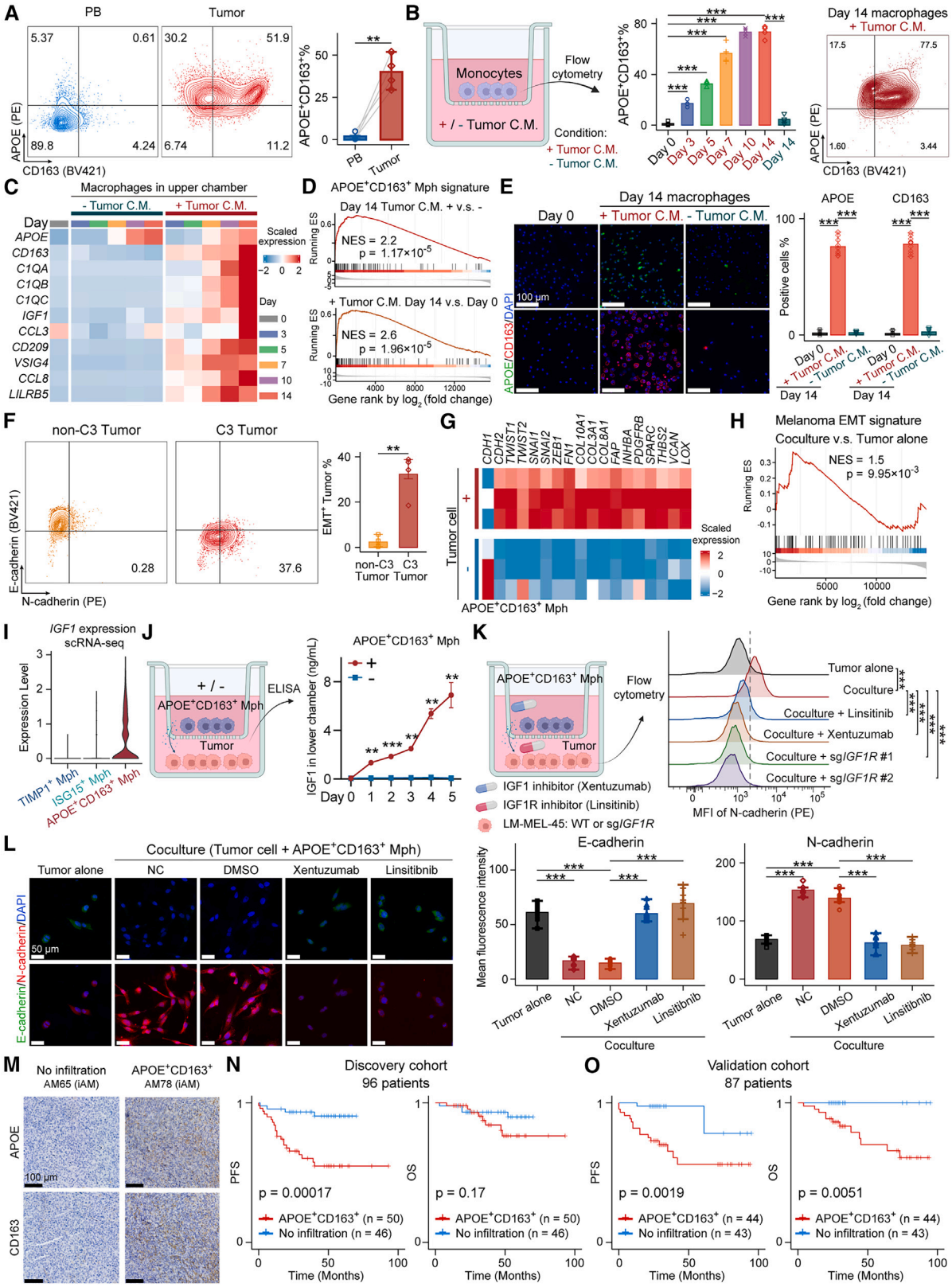

(legend on next page)

Plus X-Young Scholars Project of Peking University from the Fundamental Research Funds for the Central Universities (to R.X.). The graphical abstract, Figures 1A, 3P, 8B, 8J, and 8K were created with BioRender.com.

AUTHOR CONTRIBUTIONS

Conceptualization, H.Li, N.Z., and R.X.; methodology, R.X., H.Liu, J.G., and J.C.; validation, H.Liu, J.G., M.F., and Y.T.; formal analysis, R.X., H.Liu, M.F., J.C., Y.T., and Q.C.; investigation, N.Z., R.X., and H.Liu; resources, H.Li, J.G., C.Z., M.Z., Y.Y., and Y.W.; data curation, H.Li, H.Liu, J.G., J.Z., and G.Z.; writing – original draft, R.X., and H.Liu; writing – review & editing, H.Li, N.Z., and R.X.; visualization, H.Liu, M.F., Z.Z., and Z.M.; supervision, N.Z., H.Li, and R.X.; project administration, N.Z., H.Li, and R.X.; funding acquisition, H.Li, N.Z., and R.X.

DECLARATION OF INTERESTS

R.X., H.Li, N.Z., H.Liu, and J.G. are inventors on an issued patent (ZL 2022 1 1694419.2) regarding the prognostic prediction with APOE and CD163 for patients with AM. N.Z. is the CSO of Yunnan Baiyao Group.

Received: November 10, 2022
Revised: March 21, 2024
Accepted: April 26, 2024
Published: May 16, 2024

REFERENCES

1. Reed, R.J. (1976). New Concepts in Surgical Pathology of the Skin (John Wiley & Sons).
2. Chen, Y.A., Teer, J.K., Eroglu, Z., Wu, J.Y., Koomen, J.M., Karreth, F.A., Messina, J.L., and Smalley, K.S.M. (2020). Translational pathology, genomics and the development of systemic therapies for acral melanoma. Semin. Cancer Biol. *61*, 149–157. https://doi.org/10.1016/j.semcancer.2019.10.017.
3. Bello, D.M., Chou, J.F., Panageas, K.S., Brady, M.S., Coit, D.G., Carvajal, R.D., and Ariyan, C.E. (2013). Prognosis of acral melanoma: a series of 281 patients. Ann. Surg Oncol. *20*, 3618–3625. https://doi.org/10.1245/s10434-013-3089-0.
4. Darmawan, C.C., Jo, G., Montenegro, S.E., Kwak, Y., Cheol, L., Cho, K.H., and Mun, J.H. (2019). Early detection of acral melanoma: A review of clinical, dermoscopic, histopathologic, and molecular characteristics. J. Am. Acad. Dermatol. *81*, 805–812. https://doi.org/10.1016/j.jaad.2019.01.081.
5. Shi, Q., Liu, L., Chen, J., Zhang, W., Guo, W., Wang, X., Wang, H., Guo, S., Yue, Q., Ma, J., et al. (2022). Integrative genomic profiling uncovers therapeutic targets of acral melanoma in Asian populations. Clin. Cancer Res. *28*, 2690–2703. https://doi.org/10.1158/1078-0432.Ccr-21-3344.
6. Farshidfar, F., Rhrissorrakrai, K., Levovitz, C., Peng, C., Knight, J., Bacchiocchi, A., Su, J., Yin, M., Sznol, M., Ariyan, S., et al. (2022). Integrative molecular and clinical profiling of acral melanoma links focal amplification of 22q11.21 to metastasis. Nat. Commun. *13*, 898. https://doi.org/10.1038/s41467-022-28566-4.
7. Newell, F., Wilmott, J.S., Johansson, P.A., Nones, K., Addala, V., Mukhopadhyay, P., Broit, N., Amato, C.M., Van Gulick, R., Kazakoff, S.H., et al. (2020). Whole-genome sequencing of acral melanoma reveals genomic complexity and diversity. Nat. Commun. *11*, 5259. https://doi.org/10.1038/s41467-020-18988-3.
8. Newell, F., Johansson, P.A., Wilmott, J.S., Nones, K., Lakis, V., Pritchard, A.L., Lo, S.N., Rawson, R.V., Kazakoff, S.H., Colebatch, A.J., et al. (2022). Comparative genomics provides etiological and biological insights into melanoma subtypes. Cancer Discov. *12*, 2856–2879. https://doi.org/10.1158/2159-8290.Cd-22-0603.
9. Moon, K.R., Choi, Y.D., Kim, J.M., Jin, S., Shin, M.H., Shim, H.J., Lee, J.B., and Yun, S.J. (2018). Genetic Alterations in Primary Acral Melanoma and Acral Melanocytic Nevus in Korea: Common Mutated Genes Show Distinct Cytomorphological Features. J. Invest. Dermatol. *138*, 933–945. https://doi.org/10.1016/j.jid.2017.11.017.
10. Shain, A.H., and Bastian, B.C. (2016). From melanocytes to melanomas. Nat. Rev. Cancer *16*, 345–358. https://doi.org/10.1038/nrc.2016.37.
11. Park, H.S., and Cho, K.H. (2010). Acral lentiginous melanoma *in situ*: a diagnostic and management challenge. Cancers *2*, 642–652. https://doi.org/10.3390/cancers2020642.
12. Centeno, P.P., Pavet, V., and Marais, R. (2023). The journey from melanocytes to melanoma. Nat. Rev. Cancer *23*, 372–390. https://doi.org/10.1038/s41568-023-00565-7.
13. Weinstock, M.A., and Sober, A.J. (1987). The risk of progression of lentigo maligna to lentigo maligna melanoma. Br. J. Dermatol. *116*, 303–310. https://doi.org/10.1111/j.1365-2133.1987.tb05843.x.
14. Zahir, N., Sun, R., Gallahan, D., Gatenby, R.A., and Curtis, C. (2020). Characterizing the ecological and evolutionary dynamics of cancer. Nat. Genet. *52*, 759–767. https://doi.org/10.1038/s41588-020-0668-4.

Figure 8. Functional assays

(A) Flow cytometry plots showing APOE$^+$CD163$^+$ macrophages from matched peripheral blood (PB) and tumor tissues of AM patients ($n = 4$). The bar plot displays APOE$^+$CD163$^+$ macrophage proportions. Paired Student's t test.
(B) Co-culture system of monocytes from the PB of healthy donors and the C.M. of the LM-MEL-45 tumor cell line. The bar plot shows the induced APOE$^+$CD163$^+$ macrophage proportions at different time points and conditions. Data shown as $n = 3$ in each group. A representative flow cytometry plot is shown on the right. Student's t test.
(C) RNA expression heatmap for signature genes of APOE$^+$CD163$^+$ macrophages. $n = 3$ biological replicates for each column.
(D) Enrichment of gene signature based on GSEA analysis between the indicated groups. Permutation test, $n = 100{,}000$ permutations.
(E) Representative images showing APOE and CD163 expression of macrophages. Scale bar, 100 μm. Quantifications are shown on the right side. $n = 10$ fields per group. Student's t test.
(F) Flow cytometry plots showing epithelial-mesenchymal transition (EMT) tumor cells from C3 and non-C3 AM samples ($n = 4$). The bar plot displays EMT tumor cell proportions. Student's t test.
(G) RNA expression heatmap for EMT marker genes in LM-MEL-45 cells ($n = 3$ biological replicates for each row).
(H) Enrichment of EMT signature based on GSEA analysis. Permutation test, $n = 100{,}000$ permutations.
(I) *IGF1* expression levels across macrophages subsets in scRNA-seq data.
(J) Co-culture system to assess the influence of APOE$^+$CD163$^+$ macrophages on tumor cells. IGF1 protein secreted by macrophages to the lower chamber is quantified by ELISA. Data shown as $n = 3$ per group. Student's t test.
(K) Assessment of tumor cells' EMT level in the co-culture system in (J). N-cadherin expression is quantified by flow cytometry at different conditions as indicated. Two sgRNAs (#1 and #2) were used to knock out *IGF1R* in the tumor cell line. WT, wild type. $n = 3$ per group. Student's t test.
(L) Representative images showing E-cadherin and N-cadherin expression of LM-MEL-45 tumor cells. Scale bar, 50 μm. Quantifications can be found on the right side. $n = 10$ fields per group. Student's t test.
(M) Representative IHC images of APOE and CD163 in negative (no infiltration) and positive (infiltration) patients. Scale bar, 100 μm.
(N and O) Progression-free survival, PFS, and overall survival, OS, of patients with AM in the discovery cohort (N) and validation cohort (O) stratified by APOE and CD163 staining. Log-rank test. Data are represented as mean ± SD in (A, B, E, F, and L). $^{**}p < 0.01$, $^{***}p < 0.001$. See also Figure S8 and Table S7.

15. Crosby, D., Bhatia, S., Brindle, K.M., Coussens, L.M., Dive, C., Emberton, M., Esener, S., Fitzgerald, R.C., Gambhir, S.S., Kuhn, P., et al. (2022). Early detection of cancer. Science *375*, eaay9040. https://doi.org/10.1126/science.aay9040.

16. Turajlic, S., Furney, S.J., Lambros, M.B., Mitsopoulos, C., Kozarewa, I., Geyer, F.C., Mackay, A., Hakas, J., Zvelebil, M., Lord, C.J., et al. (2012). Whole genome sequencing of matched primary and metastatic acral melanomas. Genome Res. *22*, 196–207. https://doi.org/10.1101/gr.125591.111.

17. Smalley, I., and Smalley, K.S.M. (2022). Space Is the Place: Mapping the Cell-Cell Interactions That Predict Immunotherapy Responses in Melanoma. Cancer Res. *82*, 3198–3200. https://doi.org/10.1158/0008-5472.Can-22-2192.

18. Xue, R., Zhang, Q., Cao, Q., Kong, R., Xiang, X., Liu, H., Feng, M., Wang, F., Cheng, J., Li, Z., et al. (2022). Liver tumour immune microenvironment subtypes and neutrophil heterogeneity. Nature *612*, 141–147. https://doi.org/10.1038/s41586-022-05400-x.

19. Cancer Genome Atlas Network (2015). Genomic classification of cutaneous melanoma. Cell *161*, 1681–1696. https://doi.org/10.1016/j.cell.2015.05.044.

20. Robertson, A.G., Shih, J., Yau, C., Gibb, E.A., Oba, J., Mungall, K.L., Hess, J.M., Uzunangelov, V., Walter, V., Danilova, L., et al. (2017). Integrative analysis identifies four molecular and clinical subsets in uveal melanoma. Cancer Cell *32*, 204–220.e15. https://doi.org/10.1016/j.ccell.2017.07.003.

21. Hugo, W., Zaretsky, J.M., Sun, L., Song, C., Moreno, B.H., Hu-Lieskovan, S., Berent-Maoz, B., Pang, J., Chmielowski, B., Cherry, G., et al. (2016). Genomic and Transcriptomic Features of Response to Anti-PD-1 Therapy in Metastatic Melanoma. Cell *165*, 35–44. https://doi.org/10.1016/j.cell.2016.02.065.

22. Zhang, C., Shen, H., Yang, T., Li, T., Liu, X., Wang, J., Liao, Z., Wei, J., Lu, J., Liu, H., et al. (2022). A single-cell analysis reveals tumor heterogeneity and immune environment of acral melanoma. Nat. Commun. *13*, 7250. https://doi.org/10.1038/s41467-022-34877-3.

23. Li, J., Smalley, I., Chen, Z., Wu, J.Y., Phadke, M.S., Teer, J.K., Nguyen, T., Karreth, F.A., Koomen, J.M., Sarnaik, A.A., et al. (2022). Single cell characterization of the cellular landscape of acral melanoma identifies novel targets for immunotherapy. Clin. Cancer Res. *28*, 2131–2146. https://doi.org/10.1158/1078-0432.Ccr-21-3145.

24. Hayward, N.K., Wilmott, J.S., Waddell, N., Johansson, P.A., Field, M.A., Nones, K., Patch, A.M., Kakavand, H., Alexandrov, L.B., Burke, H., et al. (2017). Whole-genome landscapes of major melanoma subtypes. Nature *545*, 175–180. https://doi.org/10.1038/nature22071.

25. Smalley, K.S.M., Teer, J.K., Chen, Y.A., Wu, J.Y., Yao, J., Koomen, J.M., Chen, W.S., Rodriguez-Waitkus, P., Karreth, F.A., and Messina, J.L. (2021). A mutational survey of acral nevi. JAMA Dermatol. *157*, 831–835. https://doi.org/10.1001/jamadermatol.2021.0793.

26. McGranahan, N., and Swanton, C. (2017). Clonal Heterogeneity and Tumor Evolution: Past, Present, and the Future. Cell *168*, 613–628. https://doi.org/10.1016/j.cell.2017.01.018.

27. van Dijk, E., van den Bosch, T., Lenos, K.J., El Makrini, K., Nijman, L.E., van Essen, H.F.B., Lansu, N., Boekhout, M., Hageman, J.H., Fitzgerald, R.C., et al. (2021). Chromosomal copy number heterogeneity predicts survival rates across cancers. Nat. Commun. *12*, 3188. https://doi.org/10.1038/s41467-021-23384-6.

28. Carter, S.L., Eklund, A.C., Kohane, I.S., Harris, L.N., and Szallasi, Z. (2006). A signature of chromosomal instability inferred from gene expression profiles predicts clinical outcome in multiple human cancers. Nat. Genet. *38*, 1043–1048. https://doi.org/10.1038/ng1861.

29. Endesfelder, D., Burrell, R., Kanu, N., McGranahan, N., Howell, M., Parker, P.J., Downward, J., Swanton, C., and Kschischo, M. (2014). Chromosomal instability selects gene copy-number variants encoding core regulators of proliferation in ER+ breast cancer. Cancer Res. *74*, 4853–4863. https://doi.org/10.1158/0008-5472.CAN-13-2664.

30. Phan, A., Touzet, S., Dalle, S., Ronger-Savlé, S., Balme, B., and Thomas, L. (2007). Acral lentiginous melanoma: histopathological prognostic features of 121 cases. Br. J. Dermatol. *157*, 311–318. https://doi.org/10.1111/j.1365-2133.2007.08031.x.

31. Shain, A.H., Yeh, I., Kovalyshyn, I., Sriharan, A., Talevich, E., Gagnon, A., Dummer, R., North, J., Pincus, L., Ruben, B., et al. (2015). The genetic evolution of melanoma from precursor lesions. N. Engl. J. Med. *373*, 1926–1936. https://doi.org/10.1056/NEJMoa1502583.

32. Xue, R., Li, R., Guo, H., Guo, L., Su, Z., Ni, X., Qi, L., Zhang, T., Li, Q., Zhang, Z., et al. (2016). Variable intra-tumor genomic heterogeneity of multiple lesions in patients with hepatocellular carcinoma. Gastroenterology *150*, 998–1008. https://doi.org/10.1053/j.gastro.2015.12.033.

33. Xiang, X., Liu, Z., Zhang, C., Li, Z., Gao, J., Zhang, C., Cao, Q., Cheng, J., Liu, H., Chen, D., et al. (2021). IDH mutation subgroup status associates with intratumor heterogeneity and the tumor microenvironment in intrahepatic cholangiocarcinoma. Adv. Sci. *8*, e2101230. https://doi.org/10.1002/advs.202101230.

34. Hu, Z., Li, Z., Ma, Z., and Curtis, C. (2020). Multi-cancer analysis of clonality and the timing of systemic spread in paired primary tumors and metastases. Nat. Genet. *52*, 701–708. https://doi.org/10.1038/s41588-020-0628-z.

35. Guo, L., Yi, X., Chen, L., Zhang, T., Guo, H., Chen, Z., Cheng, J., Cao, Q., Liu, H., Hou, C., et al. (2022). Single cell DNA sequencing reveals punctuated and gradual clonal evolution in hepatocellular carcinoma. Gastroenterology *162*, 238–252. https://doi.org/10.1053/j.gastro.2021.08.052.

36. Obradovic, A., Chowdhury, N., Haake, S.M., Ager, C., Wang, V., Vlahos, L., Guo, X.V., Aggen, D.H., Rathmell, W.K., Jonasch, E., et al. (2021). Single-cell protein activity analysis identifies recurrence-associated renal tumor macrophages. Cell *184*, 2988–3005.e16. https://doi.org/10.1016/j.cell.2021.04.038.

37. Pozniak, J., Pedri, D., Landeloos, E., Van Herck, Y., Antoranz, A., Vanwynsberghe, L., Nowosad, A., Roda, N., Makhzami, S., Bervoets, G., et al. (2024). A TCF4-dependent gene regulatory network confers resistance to immunotherapy in melanoma. Cell *187*, 166–183.e25. https://doi.org/10.1016/j.cell.2023.11.037.

38. Wouters, J., Kalender-Atak, Z., Minnoye, L., Spanier, K.I., De Waegeneer, M., Bravo González-Blas, C., Mauduit, D., Davie, K., Hulselmans, G., Najem, A., et al. (2020). Robust gene expression programs underlie recurrent cell states and phenotype switching in melanoma. Nat. Cell Biol. *22*, 986–998. https://doi.org/10.1038/s41556-020-0547-3.

39. Tsoi, J., Robert, L., Paraiso, K., Galvan, C., Sheu, K.M., Lay, J., Wong, D.J.L., Atefi, M., Shirazi, R., Wang, X., et al. (2018). Multi-stage differentiation defines melanoma subtypes with differential vulnerability to drug-induced iron-dependent oxidative stress. Cancer Cell *33*, 890–904.e5. https://doi.org/10.1016/j.ccell.2018.03.017.

40. Dongre, A., and Weinberg, R.A. (2019). New insights into the mechanisms of epithelial-mesenchymal transition and implications for cancer. Nat. Rev. Mol. Cell Biol. *20*, 69–84. https://doi.org/10.1038/s41580-018-0080-4.

41. Hara, T., Chanoch-Myers, R., Mathewson, N.D., Myskiw, C., Atta, L., Bussema, L., Eichhorn, S.W., Greenwald, A.C., Kinker, G.S., Rodman, C., et al. (2021). Interactions between cancer cells and immune cells drive transitions to mesenchymal-like states in glioblastoma. Cancer Cell *39*, 779–792.e11. https://doi.org/10.1016/j.ccell.2021.05.002.

42. Vahid, M.R., Brown, E.L., Steen, C.B., Zhang, W., Jeon, H.S., Kang, M., Gentles, A.J., and Newman, A.M. (2023). High-resolution alignment of single-cell and spatial transcriptomes with CytoSPACE. Nat. Biotechnol. *41*, 1543–1548. https://doi.org/10.1038/s41587-023-01697-9.

43. Jin, S., Guerrero-Juarez, C.F., Zhang, L., Chang, I., Ramos, R., Kuan, C.H., Myung, P., Plikus, M.V., and Nie, Q. (2021). Inference and analysis of cell-cell communication using CellChat. Nat. Commun. *12*, 1088. https://doi.org/10.1038/s41467-021-21246-9.

44. Makohon-Moore, A.P., Lipson, E.J., Hooper, J.E., Zucker, A., Hong, J., Bielski, C.M., Hayashi, A., Tokheim, C., Baez, P., Kappagantula, R., et al. (2021). The genetic evolution of treatment-resistant cutaneous, acral, and uveal melanomas. Clin. Cancer Res. *27*, 1516–1525. https://doi.org/10.1158/1078-0432.CCR-20-2984.

45. Shain, A.H., Bagger, M.M., Yu, R., Chang, D., Liu, S., Vemula, S., Weier, J.F., Wadt, K., Heegaard, S., Bastian, B.C., and Kiilgaard, J.F. (2019). The genetic evolution of metastatic uveal melanoma. Nat. Genet. *51*, 1123–1130. https://doi.org/10.1038/s41588-019-0440-9.

46. Phadke, M.S., and Smalley, K.S.M. (2023). Targeting NRAS Mutations in Advanced Melanoma. J. Clin. Oncol. *41*, 2661–2664. https://doi.org/10.1200/jco.23.00205.

47. Weiss, J.M., Hunter, M.V., Cruz, N.M., Baggiolini, A., Tagore, M., Ma, Y., Misale, S., Marasco, M., Simon-Vermot, T., Campbell, N.R., et al. (2022). Anatomic position determines oncogenic specificity in melanoma. Nature *604*, 354–361. https://doi.org/10.1038/s41586-022-04584-6.

48. Pittet, M.J., Michielin, O., and Migliorini, D. (2022). Clinical relevance of tumour-associated macrophages. Nat. Rev. Clin. Oncol. *19*, 402–421. https://doi.org/10.1038/s41571-022-00620-6.

49. Bancaro, N., Cali, B., Troiani, M., Elia, A.R., Arzola, R.A., Attanasio, G., Lai, P., Crespo, M., Gurel, B., Pereira, R., et al. (2023). Apolipoprotein E induces pathogenic senescent-like myeloid cells in prostate cancer. Cancer Cell *41*, 602–619.e11. https://doi.org/10.1016/j.ccell.2023.02.004.

50. Xue, R., Chen, L., Zhang, C., Fujita, M., Li, R., Yan, S.M., Ong, C.K., Liao, X., Gao, Q., Sasagawa, S., et al. (2019). Genomic and transcriptomic profiling of combined hepatocellular and intrahepatic cholangiocarcinoma reveals distinct molecular subtypes. Cancer Cell *35*, 932–947.e8. https://doi.org/10.1016/j.ccell.2019.04.007.

51. Vasimuddin, M., Misra, S., Li, H., and Aluru, S. (2019). Efficient Architecture-Aware Acceleration of BWA-MEM for Multicore Systems. 2019 IEEE International Parallel and Distributed Processing Symposium (IPDPS). https://doi.org/10.1109/IPDPS.2019.00041.

52. Li, H., Handsaker, B., Wysoker, A., Fennell, T., Ruan, J., Homer, N., Marth, G., Abecasis, G., and Durbin, R.; 1000 Genome Project Data Processing Subgroup (2009). The Sequence Alignment/Map format and SAMtools. Bioinformatics *25*, 2078–2079. https://doi.org/10.1093/bioinformatics/btp352.

53. McKenna, A., Hanna, M., Banks, E., Sivachenko, A., Cibulskis, K., Kernytsky, A., Garimella, K., Altshuler, D., Gabriel, S., Daly, M., and DePristo, M.A. (2010). The Genome Analysis Toolkit: a MapReduce framework for analyzing next-generation DNA sequencing data. Genome Res. *20*, 1297–1303. https://doi.org/10.1101/gr.107524.110.

54. Cibulskis, K., Lawrence, M.S., Carter, S.L., Sivachenko, A., Jaffe, D., Sougnez, C., Gabriel, S., Meyerson, M., Lander, E.S., and Getz, G. (2013). Sensitive detection of somatic point mutations in impure and heterogeneous cancer samples. Nat. Biotechnol. *31*, 213–219. https://doi.org/10.1038/nbt.2514.

55. Koboldt, D.C., Larson, D.E., and Wilson, R.K. (2013). Using VarScan 2 for Germline Variant Calling and Somatic Mutation Detection. Curr. Protoc. Bioinformatics *44*, 15.4.1–15.4.17. https://doi.org/10.1002/0471250953.bi1504s44.

56. Kim, S., Scheffler, K., Halpern, A.L., Bekritsky, M.A., Noh, E., Källberg, M., Chen, X., Kim, Y., Beyter, D., Krusche, P., and Saunders, C.T. (2018). Strelka2: fast and accurate calling of germline and somatic variants. Nat. Methods *15*, 591–594. https://doi.org/10.1038/s41592-018-0051-x.

57. Wang, K., Li, M., and Hakonarson, H. (2010). ANNOVAR: functional annotation of genetic variants from high-throughput sequencing data. Nucleic Acids Res. *38*, e164. https://doi.org/10.1093/nar/gkq603.

58. Thorvaldsdottir, H., Robinson, J.T., and Mesirov, J.P. (2013). Integrative Genomics Viewer (IGV): high-performance genomics data visualization and exploration. Briefings Bioinf. *14*, 178–192. https://doi.org/10.1093/bib/bbs017.

59. Lawrence, M.S., Stojanov, P., Polak, P., Kryukov, G.V., Cibulskis, K., Sivachenko, A., Carter, S.L., Stewart, C., Mermel, C.H., Roberts, S.A., et al. (2013). Mutational heterogeneity in cancer and the search for new cancer-associated genes. Nature *499*, 214–218. https://doi.org/10.1038/nature12213.

60. Martincorena, I., Raine, K.M., Gerstung, M., Dawson, K.J., Haase, K., Van Loo, P., Davies, H., Stratton, M.R., and Campbell, P.J. (2017). Universal Patterns of Selection in Cancer and Somatic Tissues. Cell *171*, 1029–1041.e21. https://doi.org/10.1016/j.cell.2017.09.042.

61. Favero, F., Joshi, T., Marquard, A.M., Birkbak, N.J., Krzystanek, M., Li, Q., Szallasi, Z., and Eklund, A.C. (2015). Sequenza: allele-specific copy number and mutation profiles from tumor sequencing data. Ann. Oncol. *26*, 64–70. https://doi.org/10.1093/annonc/mdu479.

62. Talevich, E., Shain, A.H., Botton, T., and Bastian, B.C. (2016). CNVkit: Genome-Wide Copy Number Detection and Visualization from Targeted DNA Sequencing. PLoS Comput. Biol. *12*, e1004873. https://doi.org/10.1371/journal.pcbi.1004873.

63. Mermel, C.H., Schumacher, S.E., Hill, B., Meyerson, M.L., Beroukhim, R., and Getz, G. (2011). GISTIC2.0 facilitates sensitive and confident localization of the targets of focal somatic copy-number alteration in human cancers. Genome Biol. *12*, R41. https://doi.org/10.1186/gb-2011-12-4-r41.

64. Islam, S.M.A., Díaz-Gay, M., Wu, Y., Barnes, M., Vangara, R., Bergstrom, E.N., He, Y., Vella, M., Wang, J., Teague, J.W., et al. (2022). Uncovering novel mutational signatures by *de novo* extraction with SigProfilerExtractor. Cell Genom *2*, None. https://doi.org/10.1016/j.xgen.2022.100179.

65. Rosenthal, R., McGranahan, N., Herrero, J., Taylor, B.S., and Swanton, C. (2016). DeconstructSigs: delineating mutational processes in single tumors distinguishes DNA repair deficiencies and patterns of carcinoma evolution. Genome Biol. *17*, 31. https://doi.org/10.1186/s13059-016-0893-4.

66. Roth, A., Khattra, J., Yap, D., Wan, A., Laks, E., Biele, J., Ha, G., Aparicio, S., Bouchard-Côté, A., and Shah, S.P. (2014). PyClone: statistical inference of clonal population structure in cancer. Nat. Methods *11*, 396–398. https://doi.org/10.1038/nmeth.2883.

67. Hanzelmann, S., Castelo, R., and Guinney, J. (2013). GSVA: gene set variation analysis for microarray and RNA-seq data. BMC Bioinf. *14*, 7. https://doi.org/10.1186/1471-2105-14-7.

68. Paradis, E., and Schliep, K. (2019). ape 5.0: an environment for modern phylogenetics and evolutionary analyses in R. Bioinformatics *35*, 526–528. https://doi.org/10.1093/bioinformatics/bty633.

69. Dobin, A., Davis, C.A., Schlesinger, F., Drenkow, J., Zaleski, C., Jha, S., Batut, P., Chaisson, M., and Gingeras, T.R. (2013). STAR: ultrafast universal RNA-seq aligner. Bioinformatics *29*, 15–21. https://doi.org/10.1093/bioinformatics/bts635.

70. Li, B., and Dewey, C.N. (2011). RSEM: accurate transcript quantification from RNA-Seq data with or without a reference genome. BMC Bioinf. *12*, 323. https://doi.org/10.1186/1471-2105-12-323.

71. Love, M.I., Huber, W., and Anders, S. (2014). Moderated estimation of fold change and dispersion for RNA-seq data with DESeq2. Genome Biol. *15*, 550. https://doi.org/10.1186/s13059-014-0550-8.

72. Yu, G., Wang, L.G., Han, Y., and He, Q.Y. (2012). clusterProfiler: an R package for comparing biological themes among gene clusters. OMICS *16*, 284–287. https://doi.org/10.1089/omi.2011.0118.

73. Liberzon, A., Birger, C., Thorvaldsdóttir, H., Ghandi, M., Mesirov, J.P., and Tamayo, P. (2015). The Molecular Signatures Database (MSigDB) hallmark gene set collection. Cell Syst. *1*, 417–425. https://doi.org/10.1016/j.cels.2015.12.004.

74. Bagaev, A., Kotlov, N., Nomie, K., Svekolkin, V., Gafurov, A., Isaeva, O., Osokin, N., Kozlov, I., Frenkel, F., Gancharova, O., et al. (2021). Conserved pan-cancer microenvironment subtypes predict response to immunotherapy. Cancer Cell *39*, 845–865.e7. https://doi.org/10.1016/j.ccell.2021.04.014.

75. Mak, M.P., Tong, P., Diao, L., Cardnell, R.J., Gibbons, D.L., William, W.N., Skoulidis, F., Parra, E.R., Rodriguez-Canales, J., Wistuba, I.I., et al. (2016). A Patient-Derived, Pan-Cancer EMT Signature Identifies Global Molecular Alterations and Immune Target Enrichment Following Epithelial-to-Mesenchymal Transition. Clin. Cancer Res. *22*, 609–620. https://doi.org/10.1158/1078-0432.CCR-15-0876.

76. Rooney, M.S., Shukla, S.A., Wu, C.J., Getz, G., and Hacohen, N. (2015). Molecular and genetic properties of tumors associated with local immune

cytolytic activity. Cell *160*, 48–61. https://doi.org/10.1016/j.cell.2014.12.033.

77. Schubert, M., Klinger, B., Klünemann, M., Sieber, A., Uhlitz, F., Sauer, S., Garnett, M.J., Blüthgen, N., and Saez-Rodriguez, J. (2018). Perturbation-response genes reveal signaling footprints in cancer gene expression. Nat. Commun. *9*, 20. https://doi.org/10.1038/s41467-017-02391-6.
78. Yoshihara, K., Shahmoradgoli, M., Martínez, E., Vegesna, R., Kim, H., Torres-Garcia, W., Treviño, V., Shen, H., Laird, P.W., Levine, D.A., et al. (2013). Inferring tumour purity and stromal and immune cell admixture from expression data. Nat. Commun. *4*, 2612. https://doi.org/10.1038/ncomms3612.
79. Newman, A.M., Liu, C.L., Green, M.R., Gentles, A.J., Feng, W., Xu, Y., Hoang, C.D., Diehn, M., and Alizadeh, A.A. (2015). Robust enumeration of cell subsets from tissue expression profiles. Nat. Methods *12*, 453–457. https://doi.org/10.1038/nmeth.3337.
80. Aran, D., Hu, Z., and Butte, A.J. (2017). xCell: digitally portraying the tissue cellular heterogeneity landscape. Genome Biol. *18*, 220. https://doi.org/10.1186/s13059-017-1349-1.
81. Hao, Y., Hao, S., Andersen-Nissen, E., Mauck, W.M., 3rd, Zheng, S., Butler, A., Lee, M.J., Wilk, A.J., Darby, C., Zager, M., et al. (2021). Integrated analysis of multimodal single-cell data. Cell *184*, 3573–3587.e29. https://doi.org/10.1016/j.cell.2021.04.048.
82. Azizi, E., Carr, A.J., Plitas, G., Cornish, A.E., Konopacki, C., Prabhakaran, S., Nainys, J., Wu, K., Kiseliovas, V., Setty, M., et al. (2018). Single-Cell Map of Diverse Immune Phenotypes in the Breast Tumor Microenvironment. Cell *174*, 1293–1308.e36. https://doi.org/10.1016/j.cell.2018.05.060.
83. Tickle, T., Tirosh, I., Georgescu, C., Brown, M., and Haas, B. (2019). inferCNV of the Trinity CTAT Project (Klarman Cell Observatory, Broad Institute of MIT and Harvard).
84. Korsunsky, I., Millard, N., Fan, J., Slowikowski, K., Zhang, F., Wei, K., Baglaenko, Y., Brenner, M., Loh, P.R., and Raychaudhuri, S. (2019). Fast, sensitive and accurate integration of single-cell data with Harmony. Nat. Methods *16*, 1289–1296. https://doi.org/10.1038/s41592-019-0619-0.
85. Efremova, M., Vento-Tormo, M., Teichmann, S.A., and Vento-Tormo, R. (2020). CellPhoneDB: inferring cell-cell communication from combined expression of multi-subunit ligand-receptor complexes. Nat. Protoc. *15*, 1484–1506. https://doi.org/10.1038/s41596-020-0292-x.
86. Browaeys, R., Saelens, W., and Saeys, Y. (2020). NicheNet: modeling intercellular communication by linking ligands to target genes. Nat. Methods *17*, 159–162. https://doi.org/10.1038/s41592-019-0667-5.
87. Stringer, C., Wang, T., Michaelos, M., and Pachitariu, M. (2021). Cellpose: a generalist algorithm for cellular segmentation. Nat. Methods *18*, 100–106. https://doi.org/10.1038/s41592-020-01018-x.
88. Bankhead, P., Loughrey, M.B., Fernández, J.A., Dombrowski, Y., McArt, D.G., Dunne, P.D., McQuaid, S., Gray, R.T., Murray, L.J., Coleman, H.G., et al. (2017). QuPath: Open source software for digital pathology image analysis. Sci. Rep. *7*, 16878. https://doi.org/10.1038/s41598-017-17204-5.

STAR★METHODS

KEY RESOURCES TABLE

REAGENT or RESOURCE	SOURCE	IDENTIFIER
Antibodies		
Rabbit anti-human MelanA	Abcam	Cat# ab112076
Mouse anti-human CD163, clone 10D6	Abcam	Cat# ab74604; RRID: AB_128790
Rabbit anti-human ApoE, clone D17N	Cell Signaling Technologies	Cat# 13366S; RRID: AB_2798191
Mouse anti-human CD68, clone KP1	ZSGB-Bio	Cat# ZM-0060; RRID: AB_2904190
Mouse anti-human E-cadherin, clone 4A2	Cell Signaling Technologies	Cat# 14472S; RRID: AB_2728770
Rabbit anti-human N-cadherin, clone D4R1H	Cell Signaling Technologies	Cat# 13116S; RRID: AB_2687616
Rabbit anti-human FN1, clone E5H6X	Cell Signaling Technologies	Cat# 26836S; RRID: AB_2924220
Rabbitt anti-human phospho-Akt (Ser473)	Cell Signaling Technologies	Cat# 9271S; RRID: AB_329825
Rabbit anti-human phospho-p44/42 MAPK (ERK1/2) (Thr202/Tyr204)	Cell Signaling Technologies	Cat# 9101S; RRID: AB_331646
E-cadherin-BX014 (4A2C7)—ATTO 550-RX014 Kit	Akoya Biosciences	Cat# 4250021; RRID: AB_2895057
Formerly CD68-BX015 (KP1)—Alexa Fluor™ 647-RX015	Akoya Biosciences	Cat# 4550113; RRID: AB_2935894
CD20-BX007 (L26)—Alexa Fluor™ 750-RX007	Akoya Biosciences	Cat# 4450018; RRID: AB_2915939
CD8-BX026 (C8/144B)—ATTO 550-RX026	Akoya Biosciences	Cat# 4250012; RRID: AB_2915960
CD4-BX003—Alexa Fluor™ 647	Akoya Biosciences	Cat# 4550112; RRID: AB_3094499
Pan-Cytokeratin-BX019 (AE-1/AE-3)—Alexa Fluor™ 488-RX019	Akoya Biosciences	Cat# 4150020; RRID: AB_2909509
CD163-BX069—ATTO 550-RX069	Akoya Biosciences	Cat# 4250079; RRID: AB_2935895
CD3e-BX045(EP449E)—Alexa Fluor™ 647-RX045	Akoya Biosciences	Cat# 4550119; RRID: AB_2936080
Ki67-BX047 (B56)—ATTO 550-RX047	Akoya Biosciences	Cat# 4250019; RRID: AB_2895046
CD11c-BX024(118/A5)—Alexa Fluor™ 647-RX024	Akoya Biosciences	Cat# 4550114; RRID: AB_3083459
HLA-DR-BX033(EPR3692)—Alexa Fluor™ 647-RX033	Akoya Biosciences	Cat# 4550118; RRID: AB_3080864
T-bet-BX052—ATTO 550-RX052	Akoya Biosciences	Cat# 4250086
PD-L1-BX043—Alexa Fluor™ 647-RX043	Akoya Biosciences	Cat# 4550072
IFNG-BX020—ATTO 550-RX020	Akoya Biosciences	Cat# 4250062
Collagen IV-BX042—Alexa Fluor™ 647-RX042	Akoya Biosciences	Cat# 4550122; RRID: AB_2927676
Anti-APOE, clone D6E10, BSA and Azide free	Abcam	Cat# ab1906; RRID: AB_302668
Anti-IGF1R, clone EPR23027-204, BSA and Azide free	Abcam	Cat# ab267345
Anti-CD86, clone EP1158-37, BSA and Azide free	Abcam	Cat# ab269593; RRID: AB_3073666
Anti-N-cadherin, clone EPR1791-4, BSA and Azide free	Abcam	Cat# ab271856; RRID: AB_2928049
Anti-MELAN-A, clone EPR20380, BSA and Azide free	Abcam	Cat# ab222483
Anti-CDKN2A/p16INK4, clone EPR1473, BSA and Azide free	Abcam	Cat# ab186932; RRID: AB_2895712

(*Continued on next page*)

Continued

REAGENT or RESOURCE	SOURCE	IDENTIFIER
Anti-IGF1, clone SPM406, BSA and Azide free	Novus	Cat# NBP2-34409
APC/Cyanine7 anti-human CD45	BioLegend	Cat# 368516; RRID: AB_2566376
Brilliant Violet 510™ anti-human CD14	BioLegend	Cat# 301842; RRID: AB_2561379
PE anti-human APOE	BioLegend	Cat# 803405; RRID: AB_2801139
PE anti-human CD163	BioLegend	Cat# 333606; RRID: AB_1134002
Brilliant Violet 421™ anti-human CD163	BioLegend	Cat# 333612; RRID: AB_2562462
PE/Cyanine7 anti-human HLA-DR	BD Pharmingen	Cat# 560651; RRID: AB_1727528
APC anti-human MelanA, clone EPR20380	Abcam	Cat# ab225498
Brilliant Violet 421™ anti-human E-cadherin	BioLegend	Cat# 147319; RRID: AB_2750483
PE anti-human N-cadherin	BioLegend	Cat# 350806; RRID: AB_10660824
Biological samples		
Tumor, adjacent normal skin tissues and peripheral blood samples from patients diagnosed with acral melanoma	This paper	N/A
Critical commercial assays		
QIAamp DNA Micro Kit	Qiagen	Cat# 56304
DNeasy Blood & Tissue Kit	Qiagen	Cat# 69504
AllPrep DNA/RNA Mini Kit	Qiagen	Cat# 80284
CLEANNGS DNA Kit	GC biotech	Cat# CNGS-0500
SureSelectXT Human All Exon V6	Agilent Technologies	Cat# 5190-8864
VAHTS mRNA-seq v2 Library Prep Kit for Illumina	Vazyme	Cat# NR601-02
Tumor Dissociation Kit, human	Miltenyi Biotec	Cat# 130-095-929
Single Cell 3' Library and Gel Bead Kit v3.1	10X Genomics	Cat# PN-1000075
Tissue Optimization Slides and Gene Expression Slides	BMKMANU	Cat# S1000
Agilent Technologies Bioanalyzer High Sensitivity kit	Agilent Technologies	Cat# 5067-4626
Antibody conjugation kit	Akoya Biosciences	Cat# 7000009
Lipofectamine 3000 Transfection Agent	ThermoFisher	Cat# L3000015
Lymphoprep density gradient medium	STEMCELL	Cat# 07861
Zombie UV Fixable Viability Kit	BioLegend	Cat# 423108
ELISA Kit for Insulin Like Growth Factor 1	Cloud-Clone	Cat# SEA050Hu
Deposited data		
Multi-omic data of AM	This paper	GSA: PRJCA025155
Public bulk genomic and RNA data of AM	Farshidfar et al.[6]	GEO: GSE162682
Public WGS data of AM	Newell et al.[7]	EGA: EGAD00001005500
Public scRNA data of AM	Zhang et al.[22]	GEO: GSE215121
Public scRNA data of AM	Li et al.[23]	GEO: GSE189889
Public genomic data of CM	Hayward et al.[24]	EGA: EGAS00001001552
TCGA melanoma datasets	Cancer Genome Atlas Research Network	https://portal.gdc.cancer.gov/
Oligonucleotides		
IGF1R-sgRNA #1, GTGGAGAACGACCATATCCG	This paper	N/A
IGF1R-sgRNA #2, TCAGTACGCCGTTTACGTCA	This paper	N/A
NF1-sgRNA #1, AGTCAGTACTGAGCACAACA	This paper	N/A
NF1-sgRNA #2, TCTCTCTCAGTTGATTATAT	This paper	N/A

(*Continued on next page*)

Continued

REAGENT or RESOURCE	SOURCE	IDENTIFIER
Software and algorithms		
BWA-mem2 2.0pre1	Vasimuddin et al.[51]	https://github.com/bwa-mem2/bwa-mem2; RRID: SCR_022192
Samtools 1.10	Li et al.[52]	http://samtools.sourceforge.net/; RRID: SCR_002105
GATK 4.1.7.0	McKenna et al.[53]	https://software.broadinstitute.org/gatk/; RRID: SCR_001876
Mutect2	Cibulskis et al.[54]	https://software.broadinstitute.org/cancer/cga/mutect
VarScan 2.4.2	Koboldt et al.[55]	http://varscan.sourceforge.net/; RRID: SCR_006849
Strelka 2.9.10	Kim et al.[56]	https://github.com/Illumina/strelka; RRID: SCR_005109
ANNOVAR	Wang et al.[57]	http://annovar.openbioinformatics.org/en/latest/; RRID: SCR_012821
Integrative Genomics Viewer	Thorvaldsdottir et al.[58]	http://software.broadinstitute.org/software/igv/; RRID: SCR_011793
MutSigCV 1.41	Lawrence et al.[59]	https://software.broadinstitute.org/cancer/cga/mutsig
dNdScv 0.0.1.0	Martincorena et al.[60]	https://github.com/im3sanger/dndscv; RRID: SCR_017093
Sequenza 3.0.0	Favero et al.[61]	https://github.com/cran/sequenza; RRID: SCR_016662
CNVkit 0.9.7	Talevich et al.[62]	https://cnvkit.readthedocs.io/en/stable/; RRID: SCR_021917
GISTIC 2.0.23	Mermel et al.[63]	https://software.broadinstitute.org/cancer/cga/gistic; RRID: SCR_000151
SigProfilerExtractor 1.0.19	Islam et al.[64]	https://github.com/AlexandrovLab/SigProfilerExtractor
deconstructSigs 1.8.0	Rosenthal et al.[65]	https://github.com/raerose01/deconstructSigs
Pyclone 0.13.1	Roth et al.[66]	https://github.com/aroth85/pyclone; RRID: SCR_016873
GSVA 1.32.0	Hanzelmann et al.[67]	https://bioconductor.org/packages/release/bioc/html/GSVA.html; RRID: SCR_021058
ape 5.5	Paradis et al.[68]	http://ape-package.ird.fr/; RRID: SCR_017343
STAR 2.7.3a	Dobin et al.[69]	https://github.com/alexdobin/STAR; RRID: SCR_004463
RSEM 1.3.3	Li et al.[70]	http://deweylab.github.io/RSEM/; RRID: SCR_013027
DESeq2 1.24.0	Love et al.[71]	http://bioconductor.org/packages/release/bioc/html/DESeq.html; RRID: SCR_015687
clusterProfiler 3.14.3	Yu et al.[72]	https://bioconductor.org/packages/release/bioc/html/clusterProfiler.html; RRID: SCR_016884
PROGENy 1.16.0	Schubert et al.[77]	https://www.bioconductor.org/packages/release/bioc/html/progeny.html
estimate 1.0.13	Yoshihara et al.[78]	https://bioinformatics.mdanderson.org/estimate/rpackage.html
CIBERSORT	Newman et al.[79]	https://cibersort.stanford.edu/; RRID: SCR_016955
xCell	Aran et al.[80]	https://xcell.ucsf.edu/

(*Continued on next page*)

Continued

REAGENT or RESOURCE	SOURCE	IDENTIFIER
survival 3.2.13	N/A	https://cran.r-project.org/web/packages/survival/index.html; RRID: SCR_021137
Cell Ranger 6.1.2	10X Genomics	https://www.10xgenomics.com/; RRID: SCR_017344
Seurat 4.0.5	Hao et al.[81]	https://cran.r-project.org/web/packages/Seurat/index.html; RRID: SCR_016341
inferCNV 1.6.0	Tickle et al.[83]	https://github.com/broadinstitute/infercnv; RRID: SCR_021140
Harmony 1.2.0	Korsunsky et al.[84]	https://github.com/immunogenomics/harmony; RRID: SCR_022206
CellPhoneDB 2.1.7	Efremova et al.[85]	https://github.com/Teichlab/cellphonedb; RRID: SCR_017054
NicheNet	Browaeys et al.[86]	https://github.com/saeyslab/nichenetr
BSTMatrix 2.3j	N/A	http://www.bmkmanu.com/portfolio/tools
cellpose 2.2.3	Stringer et al.[87]	https://github.com/MouseLand/cellpose; RRID: SCR_021716
CytoSPACE 1.0.6a0	Vahid et al.[42]	https://github.com/digitalcytometry/cytospace
CellChat 2.1.1	Jin et al.[43]	https://github.com/sqjin/CellChat; RRID: SCR_021946
QuPath 0.5.0	Bankhead et al.[88]	https://qupath.github.io/; RRID: SCR_018257
FlowJo 10.8.1	N/A	https://www.flowjo.com/
Image J 1.54f	N/A	https://imagej.net/ij/
pheatmap 1.0.12	N/A	https://www.rdocumentation.org/packages/pheatmap/versions/1.0.12; RRID: SCR_016418
Rstudio 1.3.1093	N/A	https://www.rstudio.com/products/rstudio/; RRID: SCR_000432

RESOURCE AVAILABILITY

Lead contact

Further information and requests for resources and reagents should be directed to and will be fulfilled by the lead contact, Ning Zhang (zhangning@bjmu.edu.cn).

Materials availability

This study did not generate new unique reagents.

Data and code availability

All sequencing data are available at the Genome Sequence Archive at the National Genomics Data Center (Beijing, China) under the BioProject ID: PRJCA025155. The data deposited and made public are compliant with the regulations of the Ministry of Science and Technology of China. Accession numbers for public datasets are detailed in the key resources table. We built an online website for data sharing, visualization, and re-analysis (http://meta-cancer.cn/AMatlas/). Software and code used in this study are referenced in STAR Methods and the key resources table.

EXPERIMENTAL MODEL AND STUDY PARTICIPANT DETAILS

We performed a systematic review of the case records of patients with treatment-naïve AM undergoing surgical resection at the Department of Dermatology at Peking University First Hospital (Beijing, China) from 2016 to 2023. Diagnostic pathological slides, including H&E (hematoxylin and eosin) and immunohistochemistry for Melan-A (Abcam, Cat#ab112076), were reviewed independently by two experienced dermatologists to verify the diagnoses. A total of 287 patients with treatment-naïve AM were involved, including a core discovery cohort, an expanded AMis cohort, and a validation cohort (Figure S1A). The expanded AMis cohort (139 patients) was collected for the assessment of the predictive value of adnexal involvement for AMis. The validation cohort (87 patients) was collected for the independent validation of the prognostic value of APOE and CD163 staining. Multi-omic analyses were performed on the 147 patients in the core discovery cohort, including:

(1) WES and bulk RNA seq were performed on the DNA (n=92) and RNA (n=81) obtained from 94 patients that had high-quality fresh frozen tissues, respectively;
(2) Multi-region WES was performed on 31 regions isolated from 20 patients by LCM;
(3) scRNA-seq was performed on 24 samples with fresh surgical tumor tissues;
(4) Spatial transcriptomic profiling was performed on 10 patients;
(5) Spatial protein profiling with 22-plex CODEX was performed on 12 patients with formalin-fixed paraffin-embedded (FFPE) tissues;
(6) IHC staining of APOE and CD163 was performed on 96 patients with enough FFPE tissues.

All the samples and clinical information were collected following the Declaration of Helsinki and protocols approved by the ethics committee of the Peking University First Hospital. Written informed consent was obtained from all patients enrolled in this study. The survival data of patients with AM were collected with a median follow-up time of 47 months. Detailed descriptions of the samples are provided in Table S1.

METHOD DETAILS

DNA and RNA extraction

96 fresh frozen tumor samples from 94 patients with AM were sent to simultaneous DNA and RNA extraction. For each sample, DNA and RNA were isolated following the manufacturer's protocol using AllPrep DNA/RNA Mini Kit (Qiagen, Cat#80284). After concentration quantification and fragment analysis, 92 samples and 81 samples with adequate high-quality DNA and RNA were subjected to library construction and sequencing, respectively. DNA from all peripheral blood and adjacent normal samples was isolated using the DNeasy Blood & Tissue Kit (Qiagen, Cat#69504). The concentration of DNA was quantified by Qubit 3.0 (Invitrogen) and the length of DNA segments was checked using Fragment Analyzer (Advanced Analytical Technologies) before sequencing.

LCM

31 tumor lesions from 20 patients, consisting of 8 AMis and 12 iAM, were isolated using LCM.[50] Briefly, fresh frozen tumor tissues embedded in optimal cutting temperature compound (OCT) were sliced into 4-6 reference sections (7 μm) and 15-20 LCM sections (10 μm) (PEN slide, Leica, Cat#11505158). Reference sections were stained using IHC (marker: Melan-A, Abcam, Cat#ab112076) to define the tumor regions by two experienced pathologists independently. Each lesion in the continuous LCM sections corresponding to the defined tumor region was then isolated into a specific 200 μl tube using the Leica LMD6000 Microsystem. Finally, DNA was extracted using the QIAamp DNA Micro Kit (Qiagen, Cat#56304) according to the manufacturer's protocol.

Whole exome sequencing

The sequencing library for WES was constructed using the CLEANNGS DNA Kit (GC biotech, Cat#CNGS-0500). Briefly, genomic DNA was enzymatically disrupted to a size of 180-280 bp, end polished, A-tailed, ligated with the sequencing adapter, and amplified through polymerase chain reaction (PCR). After amplification, exome regions were captured by SureSelectXT Human All Exon V6 (Agilent Technologies, Cat#5190-8864). The products were purified, quantified, and then sequenced on the Illumina NovaSeq 6000 platform to generate 150 bp paired-end reads.

Somatic mutation calling

Paired-end Illumina reads were aligned to human genome hg19 (UCSC) using BWA-mem2 (v2.0pre1)[51] with default parameters. SAM files were then converted to BAM files and sorted by chromosomal coordinates using Samtools (v1.10).[52] The Genome Analysis Toolkit (GATK v4.1.7.0)[53] was utilized to remove PCR duplicates and recalibrate the base quality score. The mean coverages of WES were 326× and 313× for tumor samples and normal samples, respectively.

For LCM samples, point mutations and indels were identified using Mutect2[54] embedded in GATK, VarScan (v2.4.2),[55] and Strelka (v2.9.10).[56] All variants were annotated with ANNOVAR.[57] High-confidence point mutations and indels were determined according to the following criteria: (1) at least 10× coverage was required in the normal sample of each patient bearing no more than 1× mutation coverage; (2) at least 10× total coverage was required in tumor samples with at least 3× mutation coverage was required; (3) variants listed in dbSNP 138 were removed unless they were documented in the Catalog of Somatic Mutations in Cancer (COSMIC) database; (4) variants recorded in the National Heart, Lung, and Blood Institute Exome Sequencing Project were excluded. Finally, variants identified by at least 2 of 3 callers were kept after filtering.

For the remaining samples, variants were detected by Mutect2 and VarScan and were annotated and filtered in the same way. Point mutations identified by Mutect2 and indels supported by both Mutect2 and VarScan were retained. Indels were manually checked via the Integrative Genomics Viewer.[58] Since germline samples (peripheral blood or adjacent normal) were not available for 14 samples (listed in Table S1), mutations were called by Mutect2 using the panel of normal as a reference created from pooled normal samples in this study. The variants of these 14 samples were excluded from significantly mutated gene identification and mutational signature analysis. All nonsynonymous somatic mutations identified in these samples are listed in Table S2.

Significantly mutated gene

Significantly mutated genes (SMG, also known as potential driver genes) were determined by MutSigCV (v1.41)[59] and dNdScv (v0.0.1.0).[60] Briefly, all variants, including synonymous and nonsynonymous variants, were passed to MutSigCV and dNdScv with default parameters to identify significantly enriched genes and detect genes under positive selection, respectively. Genes with a q value less than 0.1 were declared significant. MutSigCV identified 4 SMGs (*NPIPB9*, *NRAS*, *RBMX,* and *C6orf201*) and dNdScv identified 1 SMG (*NRAS*), thus *NRAS* was the only SMG supported by both algorithms.

Copy number alteration

Tumor ploidy, cellularity, and allelic-specific copy number of tumor samples that had paired normal samples were inferred by Sequenza (v3.0.0)[61] with default parameters. For dual-extracted samples, since the lack of peripheral blood and adjacent normal samples in 14 patients, pooled reference was constructed first using CNVkit (v0.9.7).[62] Then CNVkit was performed with default parameters to determine segments with abnormal copy number status in all 92 samples. After segmentation, GISTIC2.0 (Genomic Identification of Significant Targets in Cancer, v2.0.23)[63] was applied to identify recurrent focal gain and loss regions. For LCM samples, copy number alterations of each tumor region were determined by CNVkit using paired normal samples as reference.

Mutational signature

De novo mutational signatures were extracted from 98 samples with available paired normal samples. For LCM patients, mutations called in all regions from the same patient were assigned to a pseudo-mixed sample for tumor mutation burden analysis and signature extraction. The trinucleotide substitution context matrix of all single-nucleotide variants was used as input for SigProfilerExtractor (v1.0.19)[64] to accomplish mutational signatures modeling using non-negative matrix factorization. Three stable signatures termed signature A, B, and C were deciphered. The cosine similarity between three signatures and COSMIC single base substitution signatures was calculated to presume the corresponding potential etiological factors. Profiling of COSMIC signatures was performed using deconstructSigs (v1.8.0).[65]

CCF and subclonal structure

CCF of all mutations was estimated and the subclonal structure of each sample was then inferred based on the Bayesian clustering method using Pyclone (v0.13.1).[66] Tumor purity and allelic-specific copy numbers obtained from Sequenza were utilized. 14 tumor-only samples were excluded. Mutations with CCF greater than or equal to 0.75 were considered clonal mutations, and others were subclonal mutations.

Next, the CE and SD patterns are determined for the regional expansion of iAM after the vertical invasion. This analysis focuses on the private mutations in Syn_iAM for a certain patient. If these private mutations exhibited a subclonal peak (< 0.75), it means these tumor cells are acquiring new subclones, and hence categorized as SD. By contrast, if the private mutations are all clonal and only exhibit a clonal peak, it means these tumor cells are not acquiring new subclones and remain a highly clonal structure. Therefore, these samples are defined as CE.

Scores assessing genomic instability

(1) wGII. The wGII score is calculated based on each sample's CNA profile (CNVkit) as previously described.[29] Briefly, the ploidy is determined first as the weighted integer copy number by the lengths and copy numbers of segments. Then the percentage of gained and lost regions over the full length of each autosomal chromosome is calculated. The wGII score is defined as the average percentages over the 22 autosomal chromosomes.

(2) CNH-DNA. CNH-DNA score is a scalable measure of intertumoral heterogeneity and genomic instability from copy-number profiling. CNH-DNA is defined as the minimum of the mean distances of segments to the closest integer copy number over all possible combinations of ploidies and purities. The CNH-DNA score of each WES sample is calculated as previously described.[27]

(3) CIN-RNA. CIN-RNA score measures aneuploidy in tumor samples based on coordinated aberrations in expression of genes localized to each chromosomal region.[28] CIN-RNA score is calculated using the reported CIN signature (70 genes) by the single sample gene set enrichment analysis (ssGSEA) method integrated implanted in the R package GSVA (v1.32.0).[67]

Phylogenetic tree

Phylogenetic tree of multiple lesions from the same patient is constructed with the R package ape (v5.5).[68] Briefly, mutations (including point mutations and indels) in each patient were converted into a binary mutation matrix where 0 denotes absent and 1 denotes present (lesions in rows and mutations in columns, the zero vector was used as the root of the tree). After matrix construction, the phylogenetic tree of each patient was built based on the neighbor-joining method. The phylogenetic trees were further optimized using Adobe Illustrator. Trees based on all variations including non-synonymous and synonymous variations are used in this study. The data for the phylogenetic trees of CM is collected from a previous study.[31]

Bulk RNA sequencing

A total amount of 2 μg RNA per sample was used for transcriptomic sequencing library construction. Quality control of RNA, including RNA degradation, contamination, concentration, and integrity, was performed. The libraries were built using VAHTS mRNA-seq v2 Library Prep Kit (Vazyme, Cat#NR601-02). The final libraries (~ 350 bp) assessed by Agilent Bioanalyzer/Fragment Analyzer 5300 were sent for sequencing on the Illumina NovaSeq 6000 platform to generate 150 bp paired-end reads. Sequenced reads were aligned to human genome hg19 (GENCODE) using STAR (v2.7.3a).[69] The row count and transcripts per million (TPM) of each gene were quantified by RSEM (v1.3.3).[70] Only protein-coding genes were retained for downstream analysis. After removing transcripts with 0 value in all samples, the TPM and count of genes assigned by multiple transcripts were determined by the average expression of these transcripts. TPM values of all genes were further recalculated to obtain a sum of 1,000,000 per sample.

Hierarchical clustering

To establish a robust molecular subtype of AM, several gene expression matrices with different scale methods, multiple filtering criteria, and various clustering parameters were leveraged. Briefly, $\log_2$ (TPM + 1) normalized matrix and variance stabilizing transformed (vst) matrix from row count using 'vst' function encapsulated in the R package DESeq2 (v1.24.0)[71] were obtained. The clustering results of the normalized matrics were produced by the hierarchical clustering method based on all combinations of the following three parameters: (1) sd (for filtering highly variable genes, values: 0.75, 0.8, 0.9, 1.0, 1.2, and 1.5); (2) clustering distance (distance measure method between samples, values: 'correlation', and 'euclidean'); (3) method (distance measure method between clusters, values: 'ward.D', 'ward.D2', 'complete', 'average', 'mcquitty', 'median'). Finally, a consensus cluster was generated with the vst transformed matrix while sd, clustering distance, and method were assigned as 1.0, 'correlation', and 'ward.D2', respectively.

Pathway and signature analysis

Differential expression analyses based on bulk RNA-seq data were performed by DESeq2 using the raw count matrix. Enrichment analysis was performed using the Gene Ontology (GO), Kyoto Encyclopedia of Genes and Genomes (KEGG), and Reactome pathway database. Gene Set Enrichment Analysis (GSEA) was performed using the R package clusterProfiler (v3.14.3).[72] The normalized enrichment score (NES) and p-value of Hallmark pathway gene sets[73] were determined by GSEA with 10,000 random permutations of gene labels.

To characterize the expression signatures in each subtype, the relative gene signature enrichment scores were calculated using ssGSEA. 29 functional gene expression signatures (Fges) of TME were collected from the previous study.[74] The EMT score was calculated as previously described.[75] Cytolytic activity was defined as the average expression level of *GZMA* and *PRF1*.[76] Pathway activities were inferred by the R package PROGENy (v1.16.0).[77] The immune score was estimated by the R "estimate" package (v1.0.13).[78]

TME analysis

To determine the abundances of different cell types comparable at both the intra-sample and inter-sample levels, CIBERSORT[79] and xCell[80] were utilized to estimate the relative cell composition and enrichment score, respectively. The deconvolution algorithm embedded in CIBERSORT was run for 1,000 permutations using the TPM matrix as input. The enrichment scores of 64 different cell types were calculated using ssGSEA based on signatures provided by xCell.

Single-cell RNA sequencing

Fresh surgically resected tumor tissues were minced into pieces and digested immediately to single-cell suspension using the Tumor Dissociation Kit, human (Miltenyi Biotec, Cat#130-095-929). After the quality check upon cell viability and cell concentration, single cells were loaded for single-cell RNA-seq library preparation according to the manufacturer's instruction using the 10X Chromium Single Cell 3' Library and Gel Bead Kit v3.1 (10X Genomics, Cat#PN-1000075). The libraries were sent for sequencing based on the Illumina NovaSeq 6000 platform with a depth of at least 100,000 reads per cell to generate paired-end 150 bp reads (Capitalbio Technology).

For each sample, the feature-barcode matrix was generated using the standard pipeline embedded in Cell Ranger software (v6.1.2) with GRCh38 as a reference. All matrices from all patients were further merged and analyzed using the R package Seurat (v4.0.5)[81] based on the R (v4.0.3) programming environment. Cells with < 200 features or > 6,000 features or > 20% reads mapped to mitochondrial genes were filtered out from the downstream analysis. CellCycle scores, including G1, G2/M, and S scores, were calculated by the 'CellCycleScoring' function, and no significant cell-cycle heterogeneity was observed. Then the count matrix was normalized and scaled by a regularized negative binomial regression and the sequencing depth and percentage of reads mapped to mitochondrial genes were regressed out using the 'SCTransform' function. Expression of the top 3,000 variable genes, except mitochondrial genes, ribosome genes, and heat shock protein genes,[18] was utilized for dimensionality reduction by principal components analysis, and the first 20 PCs were selected for the following clustering.

Cell type annotation

Two-step clustering was used to determine cell types in this study. Broad cell identities were assigned through low-resolution clustering by the 'FindClusters' function at a resolution of 0.1 after removing doublets and following differential expression analysis by the 'FindAllMarkers' function with default parameters. A total of 19 clusters were generated. Melanoma cells are made up of 5 clusters

(clusters 1, 6, 8, 9, and 15) and highly expressed *PMEL*, *TYRP1*, *MLANA*, *MITF*, and *DCT*. Myeloid cells (cluster 7) were identified by the highest expression of *LYZ* and MHC class II genes such as *HLA-DRA* and *HLA-DPB1*. Other clusters were assigned to endothelial cells (clusters 0, 16, and 18; *PECAM1*, *VWF*, *CLDN5*), smooth muscle cells (cluster 3; *ACTA2*, *TAGLN*, *TPM2*), NK/T cells (cluster 5; *PTPRC*, *CD3D*, *CD2*, *NKG7*), fibroblasts (cluster 4; *LUM*, *COL1A1*, *COL1A2*), neutrophils (cluster 14; *S100A8*, *S100A9*, *CSF3R*), eccrine sweat gland cells (ESG, cluster 13; *DCD*, *SAA1*, *LTF*) epithelial cells (cluster 2, containing both keratinocytes and epithelial cells of ESG; *KRT5*, *KRT10*, *KRT14*), mast cells (cluster 11; *TPSB2*, *CPA3*), B/plasma cells (cluster 17; *CD79A*, *MZB1*, *IGHG1*), and Schwann cells (clusters 10 and 12; *S100B*, *MPZ*, *SOX10*).

Myeloid cells were extracted and re-clustered to define subgroups in detail. Subclusters were identified at the resolution 0.9, including macrophages (*CD68*, *CD163*), Langerhans cells (*CD207*, *CD1A*, *S100B*), cDC1 (*CLEC9A*, *IDO1*, *XCR1*), cDC2_CLEC10A (*CD1C*, *CLEC10A*), cDC2_CXCL9 (*CXCL9, CXCL10,*), cDC_LAMP3 (*LAMP3*, *CCL22*), plasmacytoid DCs (pDC) (*IL3RA*, *CLEC4C*), migrating DCs (*CCR7*, *CD1C*), and cycling DCs (*MKI67*, *TOP2A*). Macrophages were further divided into five subsets, including Mph_APOE, Mph_CD163, Mph_APOE_CD163, Mph_ISG15, and Mph_TIMP1. M1 and M2 polarization scores of macrophages were calculated by the 'AddModuleScore' function.[82]

Tumor cell states

Tumor cells were first determined using the inferCNV package.[83] Then these tumor cells were subjected to 'SCTransform' and Harmony integration (by samples).[84] The first 30 PCs based on Harmony integration were used for subsequent unsupervised clustering at the resolution of 0.2. Marker genes were identified by 'FindAllMarkers' and the biological state of each cell state was assessed by pathway enrichment analysis of variable databases, including MSigDB Hallmark, Reactome, Gene Ontology, and KEGG. Scores of previously reported CM signatures or cell states were calculated by the 'AddModuleScore' function.

Pseudobulk analysis

A pseudo-bulk matrix was generated by summing up all UMI counts across all cells for each gene in each patient. Then the pseudobulk matrix was converted into a TPM matrix by adjusting the library size. The top 200 significantly upregulated genes in each molecular subtype (Table S4) were used as the subtype signatures. Patients were assigned based on the signatures for three subtypes.

Ligand-receptor interaction analysis

Ligand-receptor interactions between cells were inferred by CellPhoneDB (v2.1.7).[85] To determine the specific ligand-receptor interactions modulating the expression of the EMT tumor cells, the top 100 upregulated genes in all cell clusters were plugged into NicheNet as potential ligands.[86] The top 100 upregulated genes in EMT tumor cells served as potential receptors.

mIHC

4 μm FFPE slides were incubated into Xylene, 100% ethanol, and 95% ethanol and washed before retrieval of antigen at pH 9 and incubation of BSA. Serial staining was then performed using the AlphaTSA Multiplex IHC Kit (AXT36100031, AlphaX). In each cycle, the slides were incubated with primary antibody and then corresponding Horseradish peroxidase (HRP)-conjugated secondary antibody. Primary antibodies were CD163 (clone-10D6, Abcam, Cat#ab74604, ready-to-use), APOE (clone-D17N, Cell Signaling, Cat#13366S, 1:1000), and CD68 (ZSGB-Bio, Cat#ZM-0060, 1:500). Fluorescent images were collected using the ZEISS Axioscan7 microscope and analyzed by ZEN (v3.3).

Spatial transcriptomics sequencing

Tumor tissues resected from AM patients were immediately dissected, washed with 1× PBS, and snap-frozen in liquid nitrogen-chilled isopentane. The tissues were embedded in the OCT compound placed on the dry ice, and stored at -80°C. Sections were cut at 10 μm thickness and placed onto the chilled Tissue Optimization Slides and Gene Expression Slides (BMKMANU S1000). The Gene Expression Slide has 1-8 identical 6.8×6.8 mm capture areas, each with 2,000,000 spots containing barcoded primers. The primers are attached to the slide by the 5' end and contain a cleavage site, a T7 promoter region, a partial read 1 Illumina handle, a spot-unique spatial barcode, a unique molecular identifier (UMI), and Poly(dT)VN. The spots have a diameter of 2.5 μm and are arranged in a centered regular hexagonal grid so that each spot has six surrounding spots with a center-to-center distance of 4.8 μm. Tissue optimization, fixation, H&E staining, and imaging, were conducted according to the manufacturer's protocol. Nuclei staining was also performed and imaged for subsequent cell segmentation. After reverse transcription and spatial library construction, the library was sent for quality control and sequenced on the Illumina NovaSeq 6000 platform to generate 150 bp paired-end reads.

Spatial transcriptomics analysis

Raw sequencing files were processed with BSTMatrix (v2.3j) to perform cell segmentation and obtain spatial gene expression matrices and cell coordinates. Specifically, the GRCh38 genome was used as a reference. The DAPI-stained image was used for cell segmentation using the watershed algorithm implanted in the cellpose v2.2.3.[87] The spatial expression matrix was processed using Seurat v4.0.5. Cells with more than 100 spatial features and genes expressed in at least 5 cells were retained. The cell identity was determined by integrated assessment with both unsupervised clustering and CytoSPACE alignment v1.0.6.[42] Briefly, cells were first clustered and annotated using Seurat. Cells located within specific spatial structures were clearly defined, including eccrine sweat glands, smooth muscle cells, as well as the basal, spinosum, and granulosum layers of the epidermis. Tumor cells, immune

cells, and stromal cells located within the complex structure of the TME were further classified using CytoSPACE. The spatial cell-cell interaction was performed with CellChat v2.1.1.[43]

CODEX

CODEX was performed on FFPE tissues with the PhenoCycler Fusion machine according to the manufacturer's protocol (Akoya Biosciences). A total of 22 antibodies were used, including 15 ready-to-use oligonucleotide conjugated antibodies and 7 self-conjugated antibodies that are not commercially available (detailed in Table S6). 4 μm tissue sections were mounted on poly-L-Lysine-coated coverslips and then deparaffinized and rehydrated. The tissue-retrieval process is the same as for IHC. Tissues were then fixed using the prestaining fixing solution and then washed using tissue hydration buffer. For each coverslip, the antibody cocktail (containing Melan-A, Collagen IV, Pan-CK, E-cadherin, CD3e, CD4, CD8, CD20, CD11c, HLA-DR, CD68, CD86, CD163, N-cadherin, Ki-67, Tbet, IFNγ, PD-L1, CDKN2A, APOE, IGF1, and IGF1R) was then added to the coverslip and staining was performed in a sealed humidity chamber for 3 h. Antibodies were combined at the dilutions indicated in Table S6. After staining, coverslips were washed for 4 min by staining buffer and fixed in wells containing 1.6% paraformaldehyde for 10 min, followed by three washes in PBS. The coverslips were then incubated in ice-cold 100% methanol on ice for 5 min, followed by three washes in PBS. The fresh fixative solution was prepared immediately before final fixation, and final fixation was performed at room temperature for 20 min, followed by three washes in PBS. Next, the CODEX reporter plate containing the reporter master mix for every cycle was prepared accordingly. The CODEX multicycle reaction and image acquisition were performed. Full-resolution multi-color overlay images were imported into QuPath image analysis software (v0.5.0).[88] Areas of low quality, such as folds, dried edges, and bubbles, were excluded for further analysis. The tumor regions were identified by an experienced dermatologist (J.G.). Regions of interest were annotated and cell segmentation was performed using the cell detection algorithm implemented in QuPath with default parameters. The matrix containing the expression levels of each protein, as well as the coordinates of each cell, were exported for subsequent analysis.

Construction of stable tumor cell lines

Virus preparation in 293T cells was performed using Lipofectamine 3000 Transfection Agent (ThermoFisher, Cat#L3000015) following the manufacturer's protocol. Lentivirus was prepared by transfecting the target genes plasmids with two packaging plasmids (psPAX2 and pMD2.G) into 293T cells. After 8 hours of incubation, the medium was replaced with 10 ml DEME + 10% FBS. Lentivirus was harvested at 48h and 72h after transfection. Lentivirus was added into LM-MEL-45 cells at a 1:1 v/v ratio (5 ml) and plates were centrifuged for 1 h at 2000g and placed in the incubator at 37°C overnight. Stable tumor cells were established after 72 hours of puromycin selection.

The human acral melanoma cell line LM-MEL-45 was a gift from Dr. Jun Guo (Peking University Cancer Hospital). Induction of point mutations, including $NRAS^{Q61K}$, $NRAS^{Q61R}$, $KRAS^{G12D}$, and KIT^{L576P}, was performed by transfecting LM-MEL-45 cells with vectors containing one of the above mutations. LM-MEL-45 IGF1R-KO and NF1-KO cells were generated using CRISPR-Cas9 technology. LM-MEL-45 cells were seeded in culture dishes to achieve 70-80% confluence the next day. The lentiviral supernatant containing sgRNA was then added to the cells, along with 8 μg/ml polybrene to enhance efficiency of infection. After 24 hours, the medium was replaced with fresh medium. Infected LM-MEL-45 cells were subjected to puromycin selection (1 μg/ml) for 72 hours to isolate cells that successfully integrated the sgRNA. Puromycin-resistant cells were considered sgRNA-integrated and were subsequently used for downstream experiments. The oligonucleotide sequence of sgRNAs are listed in the key resources table.

Isolation of monocytes and macrophages

For isolation of monocytes, peripheral blood (20 ml) was collected from healthy human donors or patients with AM. Density gradient separation was performed with Lymphoprep density gradient medium (STEMCELL, Cat#07861). The layer of peripheral blood mononuclear cells was sent for isolation of $CD14^+$ cells with anti-CD14 magnetic beads (STEMCELL, Cat#19359).

For isolation of TAMs, fresh tumor tissues were cut into approximately 1 mm^3 pieces in RPMI-1640 medium (Thermo Fisher Scientific) with 10% fetal bovine serum (FBS, Gibco) and enzymatically digested using the MACS tumor dissociation kit (Miltenyi Biotec) for 1 h on a rotor at 37°C, according to the manufacturer's instructions. After filtering using the 70 μm CellStrainer (BD) in RPMI-1640 medium, the suspended cells were centrifuged at 400 g for 5 min. After removing the supernatant, cell pellets were resuspended in the sorting buffer (PBS supplemented with 2% FBS) after washing twice with PBS. Throughout the dissociation procedure, cells were maintained on ice whenever possible. The cells were then centrifuged at 400 g for 5 min with 1 ml cell suspension above 5 ml 45% Percoll (Sigma, Cat#P4937, diluted with PBS) in the middle and 5 ml 60% Percoll at the bottom in a 15 ml tube. Mononuclear cells were collected from the cell layer in the interphase between 45% and 60% Percoll. $CD14^+$ monocytes and macrophages were isolated by the magnetic-activated cell sorting using anti-CD14 magnetic beads according to the manufacturer's instructions.

Co-culture of monocytes with conditioned medium of tumor cells

The LM-MEL-45 cells were cultured in RPMI-1640 medium supplemented with 10% fetal bovine serum (FBS), 100 U/ml of penicillin, and 100 μg/ml of streptomycin (Hyclone) in a humidified incubator at 37°C with 5% CO_2. Conditioned medium from LM-MEL-45 cells

was added into the lower chamber and monocytes isolated from the peripheral blood of health donors (5×10^5) were added into the upper chamber of the 12-well plate and co-cultured for 0, 3, 5, 7, 10, and 14 days. After co-culture, macrophages were sent for flow cytometry analysis, bulk RNA-seq, and immunofluorescence.

Co-culture of tumor cells with APOE$^+$CD163$^+$ macrophages

APOE$^+$CD163$^+$ macrophages were sorted on Day 10 of the above coculture using fluorescence-activated cell sorting, including staining with CD45 (Biolegend, Cat#368516), CD14 (Biolegend, Cat#301842), APOE (Biolegend, Cat#803405), and CD163 (Biolegend, Cat#333606). APOE$^+$CD163$^+$ macrophages alone or with IGF1 inhibitor Xentuzumab (MedChemExpress, Cat# HY-P99274), were placed in the top insert of transwell (0.4 μm, Corning). *IGF1R* knocking-out LM-MEL-45 cells, wild-type cells alone or with IGF1R inhibitor Linsitinib (MedChemExpress, Cat#HY-10191), were placed in the lower chamber of a 12-well plate for 5 days. Tumor cells at Day 0 and Day 5 were sent for flow cytometry analysis, bulk RNA-seq, and immunofluorescence. The concentration of IGF1 in the supernatant of the lower chamber was determined by ELISA (Cloud-Clone, Cat#SEA050Hu).

Flow cytometry analysis

For assessing APOE$^+$CD163$^+$ macrophages, cells were stained with fluorochrome-conjugated monoclonal antibodies against CD45 (Biolegend, Cat#368516), CD14 (Biolegend, Cat#301842), HLA-DR (BD Pharmingen, Cat#560651), APOE (Biolegend, Cat#803405), and CD163 (Biolegend, Cat#333606). For assessing the EMT level of tumor cells, staining was performed using antibodies against CD45 (Biolegend, Cat#368516), E-cadherin (Biolegend, Cat#147319), and N-cadherin (Biolegend, Cat#350806). The flow cytometry data was analyzed by FlowJo v10.8.1.

Immunofluorescence of cultured cells

Cells were incubated with primary antibodies against APOE (Cell Signaling, Cat#13366S) and CD163 (Abcam, Cat#ab74604) for macrophages, as well as E-cadherin (Cell Signaling, Cat#14472S) and N-cadherin (Cell Signaling, Cat#13116S) for tumor cells, followed by incubation with Alexa Fluor 594 goat anti-rabbit IgG (H+L) and Alexa Fluor 488 donkey anti-mouse IgG (H+L) (ZSGB-Bio). The fluorescent intensity was quantified by Image J (v1.54f).

Invasion assay

Filters (8 μm pore size) precoated with matrigel (Corning) placed in 48-well Boyden chambers (Corning) were used for examining cell invasion. Wild-type, mutated, or *NF1* knocking-out LM-MEL-45 cells were placed into the upper chamber in 0.2 ml of DMEM serum-free medium (2×10^5 cells per filter). DMEM medium supplemented with 10% FBS was placed in the lower chamber as a chemoattractant. After culturing for 24 hours, cells at the lower surface of the filters were fixed in methanol for 15 min at room temperature, stained using crystal violet for 15 min, visualized, and counted by Image J.

IHC

4 μm slides of FFPE samples were placed in the oven at 65°C for 2 hours. Slides were deparaffinized in xylene 2 times (15 minutes each) and then transferred through 100%, 95%, and 75% alcohol. Endogenous peroxidase activity was blocked in the 3% H_2O_2 solution at room temperature for 10 minutes. After heat-induced antigen retrieval and incubation of blocking buffer (3% bovine serum albumin) for 1 h, incubation with primary antibodies was performed at 4°C overnight. Primary antibodies used in this study include CD163 (clone-10D6, Abcam, Cat#ab74604, ready-to-use), APOE (clone-D17N, Cell Signaling, Cat#13366S, 1:750), pERK1/2 (Thr202/Tyr204, Cell Signaling, Cat#9101S, 1:200), pAKT (Ser473, Cell Signaling, Cat#9271S, 1:100), E-Cadherin (clone-4A2, Cell Signaling, Cat#14472S, 1:100), N-Cadherin (clone-D4R1H, Cell Signaling, Cat#13116S, 1:100), and FN1 (clone-E5H6X, Cell Signaling, Cat#26836S, 1:200). Slides were washed with PBS 3 times and incubated with the secondary antibody at room temperature for 1 h. 100 μl 3,3′-diaminobenzidine (DAB) was applied to reveal the color of antibody staining. Finally, slides were dehydrated through 75%, 95%, and 100% alcohol, cleared by xylene, mounted, and observed.

Each IHC slide was reviewed by two independent pathologists (J.G. and Y.T.). For APOE and CD163, the staining of each marker was considered positive when both pathologists agreed that at least 50 positive cells were observed with a comparison to the matched negative control. Only patients with double positive staining of both APOE and CD163 were determined as positive. For pERK1/2, pAKT, E-Cadherin, N-Cadherin, and FN1, due to their continuous expression spectra reflecting the degree of EMT phenotype or the activity levels of MAPK pathway or PI3K-Akt pathway, a multi-level grading (0, 1, 2, 3, based on the staining intensity of tumor cells) was conducted to each slide. The staining score was defined as the average score of the two independent assessments. For these five markers, a staining score greater than 1 was considered positive, while a score less than or equal to 1 was considered negative.

Public datasets

Genomic datasets were obtained from Farshidfar et al.,[6] Newell et al.,[7] Hayward et al.,[24] and TCGA portal (https://portal.gdc.cancer.gov/). Bulk RNA-seq data was obtained from Farshidfar et al.[6] Public scRNA-seq datasets of AM were collected from Zhang et al.[22] and Li et al.[23]

QUANTIFICATION AND STATISTICAL ANALYSIS

Statistical analyses were performed using R (v.3.6.1). Survival analysis was performed with survival (v3.2.13) using the log-rank test. All tests were two-sided unless otherwise stated. Statistical significance was defined as p values less than 0.05 or q values less than 0.1. For all the box plots, the centerline shows the median; boxes indicate the first and third quartiles; whiskers extend 1.5 times the interquartile range; dots show all data values. Each experiment was repeated three or more times with biologically independent samples.

Cancer Cell, Volume *42*

Supplemental information

Integrative molecular and spatial analysis reveals evolutionary dynamics and tumor-immune interplay of *in situ* and invasive acral melanoma

Hengkang Liu, Jiawen Gao, Mei Feng, Jinghui Cheng, Yuchen Tang, Qi Cao, Ziji Zhao, Ziqiao Meng, Jiarui Zhang, Guohong Zhang, Chong Zhang, Mingming Zhao, Yicen Yan, Yang Wang, Ruidong Xue, Ning Zhang, and Hang Li

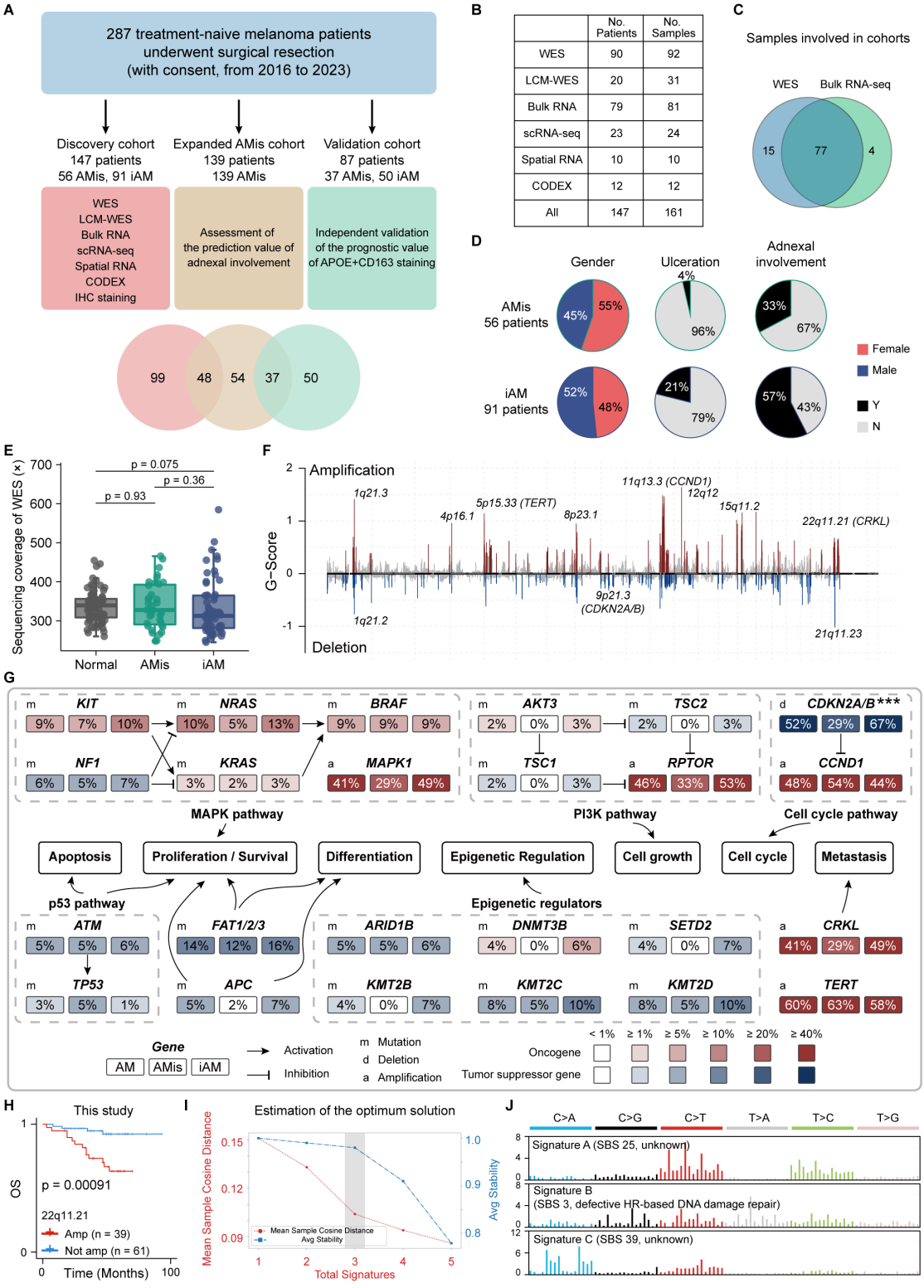

Figure S1. Cohort composition and genomic characteristics of AM, related to Figure 1

(A) Composition of AM patients in the discovery cohort, the expanded AMis cohort, and the validation cohort.
(B) Number of patients and samples involved in each sequencing platform in the discovery cohort.

(C) Samples involved in WES and bulk RNA-seq.
(D) Pie plots of clinical features between AMis and iAM patients.
(E) Box plot comparing the sequencing coverage of WES samples. The centerline shows the median; boxes indicate the first and third quartiles; whiskers extend 1.5 times the interquartile range. Mann–Whitney U test.
(F) Focal regions identified by GISTIC2 in the whole cohort.
(G) Altered frequency comparison of genes in selected signaling pathways in AM. The interactions between genes are denoted. The layout of each gene is detailed in the legend. For each gene, the statistical significance of comparisons of frequencies between AMis and iAM is indicated next to the gene. Fisher's exact test. ***$p < 0.001$. Alteration types are denoted. m, mutation; a, amplification; d, deletion.
(H) Overall survival, OS, of AM patients stratified by amplification status of 22q11.21. Log rank test.
(I) Mean sample cosine distance and average stability of each alteration of total *de novo* signature numbers extracted by SigProfilerExtractor. N = 3 was selected (indicated by the grey background) based on a comprehensive evaluation.
(J) *De novo* signatures identified in AM.

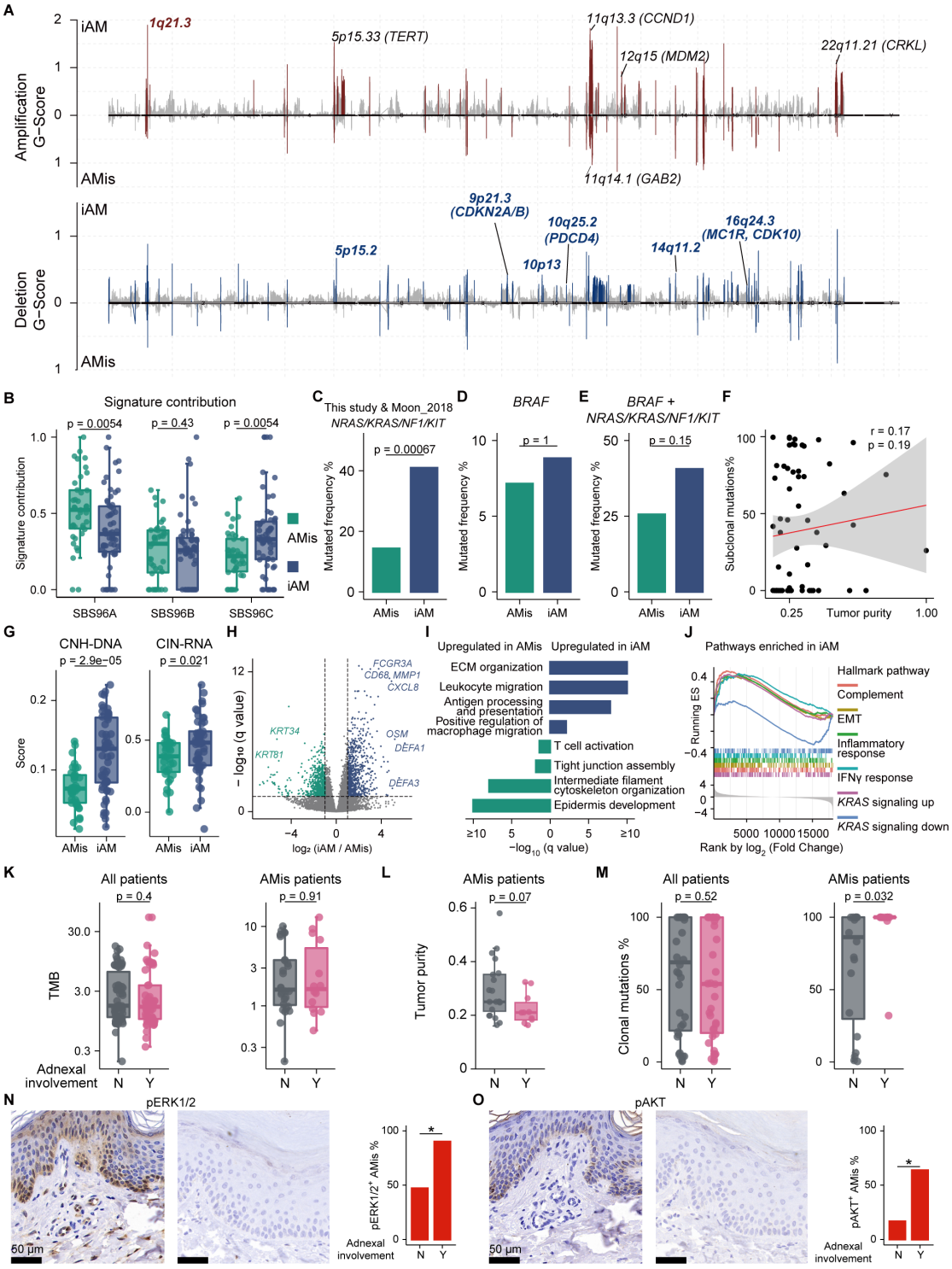

Figure S2. Genomic and transcriptomic comparison between AMis and iAM, related to Figure 2

(A) Focal amplifications (top) and deletions (bottom) among AMis and iAM samples. In each panel, regions identified in AMis and iAM samples are located on the upper and lower sides of the axis, respectively. Cytobands exhibiting significantly different frequencies ($q < 0.1$) are annotated in bold. Red, amplification; blue, deletion; black, other cytobands of interest. Fisher's exact test.

(B) Contributions of three *de novo* signatures between AMis and iAM. Mann–Whitney

U test.
(C) Bar plot comparing the mutated frequency of invasion-preferred drivers among AMis and iAM samples from this study and Moon *et al*. Fisher's exact test.
(D and E) Bar plot comparing the mutated frequency of *BRAF* (D) or combinatory mutated frequency of *BRAF* and invasion-preferred drivers (E) between AMis and iAM. Fisher's exact test.
(F) Correlation between the tumor purity and the proportion of subclonal mutations. Spearman correlation test.
(G) Box plots showing the CNH-DNA (left) and CIN-RNA score (right) between AMis and iAM. Mann–Whitney U test.
(H) Differentially expressed genes between iAM and AMis. Blue, upregulated in iAM; green, upregulated in AMis.
(I) GO terms enriched in iAM and AMis.
(J) Hallmark pathways significantly dysregulated in iAM samples.
(K) Box plots showing the tumor mutational burden (TMB) of all patients (left) or AMis patients (right) with (Y) or without (N) adnexal involvement. Mann–Whitney U test.
(L) Box plots showing the tumor purity of AMis patients (right) with or without adnexal involvement. Mann–Whitney U test.
(M) Box plots showing the frequency of clonal mutations of all patients (left) or AMis patients (right) with or without adnexal involvement. Mann–Whitney U test.
(N and O) Representative images showing staining results of pERK1/2 (N) and pAKT (O) in AMis patients. Statistical results are on the right. Scale bar, 50 μm. One-sided Fisher's exact test. *$p < 0.05$.
Data are represented as boxplots in (B, G, K-M). The centerline shows the median; boxes indicate the first and third quartiles; whiskers extend 1.5 times the interquartile range.

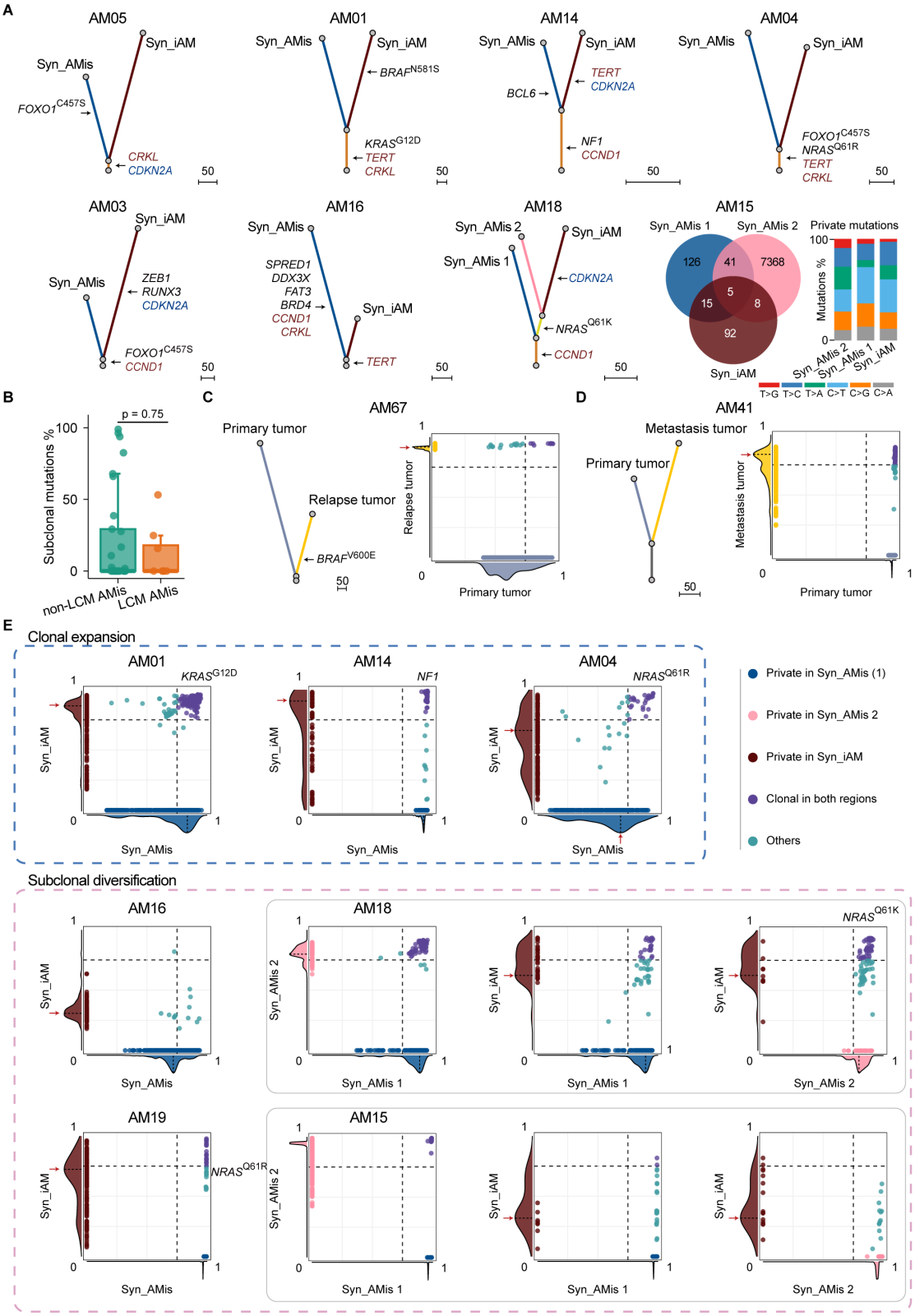

Figure S3. Phylogenetic trees and CCF plots of AM, related to Figure 3

(A) Phylogenetic trees of AM with two or more regions. The length of each line is proportional to the number of mutations. Scale bar, 50 mutations. Black, mutation; red, copy number gain; blue, copy number loss. Stacked bar plot showing the mutational spectrum of private variants in each region from AM15.

(B) Proportion of subclonal mutations of LCM-captured AMis regions compared to non-LCM-captured AMis tumors. The centerline shows the median; boxes indicate the first and third quartiles; whiskers extend 1.5 times the interquartile range. Mann–Whitney U test.
(C and D) Phylogenetic trees and CCF plots of patients AM67 (C) and AM41 (D). Gray, primary tumor; yellow, relapse/metastasis tumor.
(E) Pairwise CCF plots of mutations. Patients were grouped by patterns.

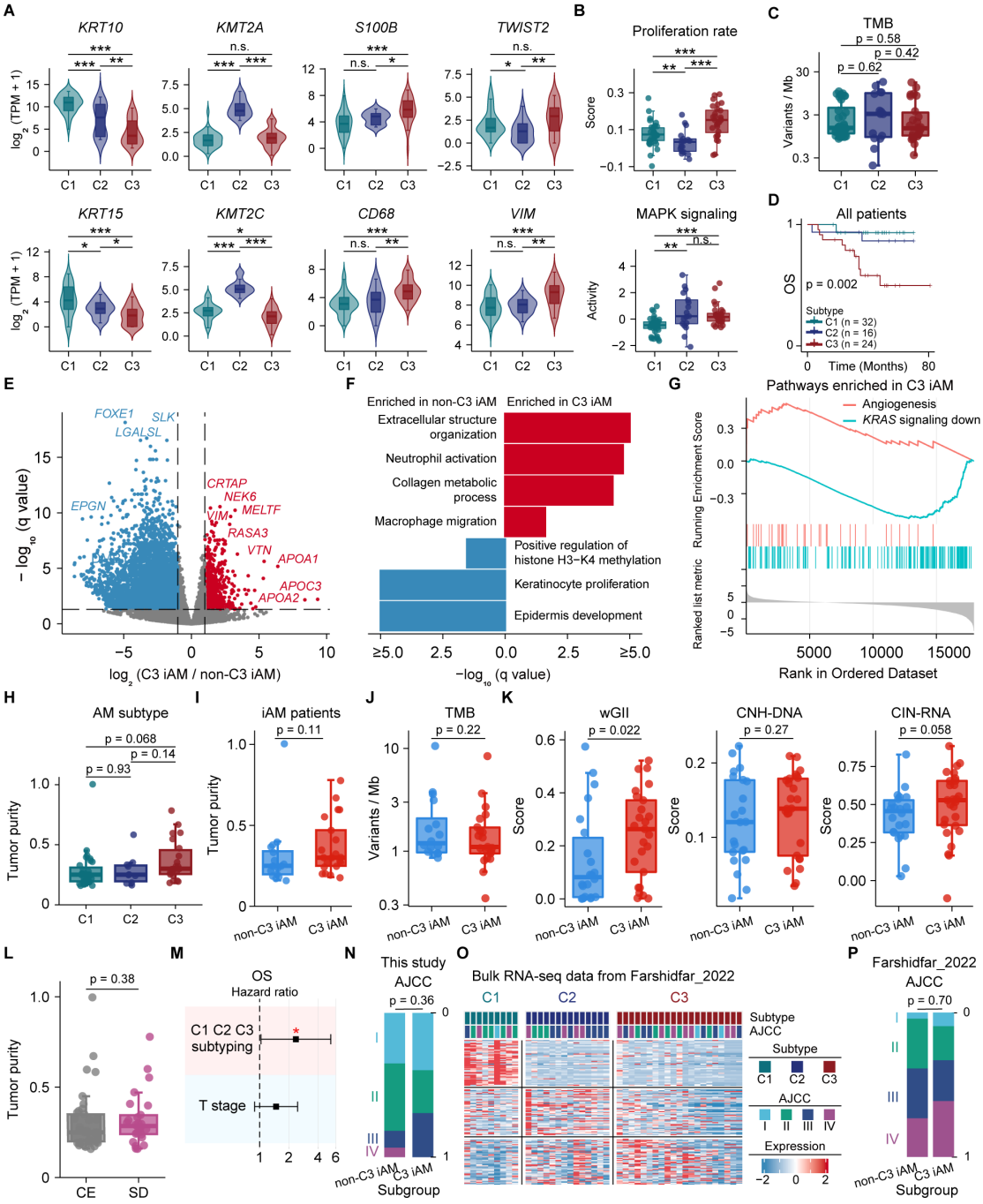

Figure S4. Genomic and transcriptomic characteristics of AM subtypes, related to Figure 4

(A-C) Level of marker genes expression (A), proliferation and MAPK (B), and TMB (C) in each subtype. Mann–Whitney U test.
(D) Overall survival, OS, of patients among the three subtypes. Log rank test.
(E) Differentially expressed genes between C3 iAM and non-C3 (C1 & C2) iAM. Red, upregulated in C3; blue, downregulated in C3 iAM.
(F) GO terms enriched in C3 iAM and non-C3 iAM.
(G) Hallmark pathways enriched in C3 iAM.
(H and I) Box plots comparing tumor purity among three subtypes (H) and iAM subtypes (I). Mann–Whitney U test.

(J) Box plot showing TMB between C3 iAM and non-C3 iAM. Mann–Whitney U test.
(K) Box plots showing scores of genomic instability among C3 iAM and non-C3 iAM, including the wGII, CNH-DNA, and CIN-RNA score. One-sided Mann–Whitney U test.
(L) Tumor purity between CE and SD samples. Mann–Whitney U test.
(M) Forest plot showing multivariate Cox regression analysis of OS for AM.
(N) Stacked bar plot showing the AJCC stage of C3 iAM and non-C3 iAM samples in this study. Chi-square test.
(O) Heatmap showing the subtypes of AM samples based on bulk RNA-seq data collected from Farshidfar *et al*.
(P) Stacked bar plot showing the AJCC stage of C3 iAM and non-C3 iAM samples in the Farshidfar *et al*. cohort. Chi-square test.
Data are represented as boxplots in (A-C, and H-L). The centerline shows the median; boxes indicate the first and third quartiles; whiskers extend 1.5 times the interquartile range. *$p < 0.05$, **$p < 0.01$, ***$p < 0.001$.

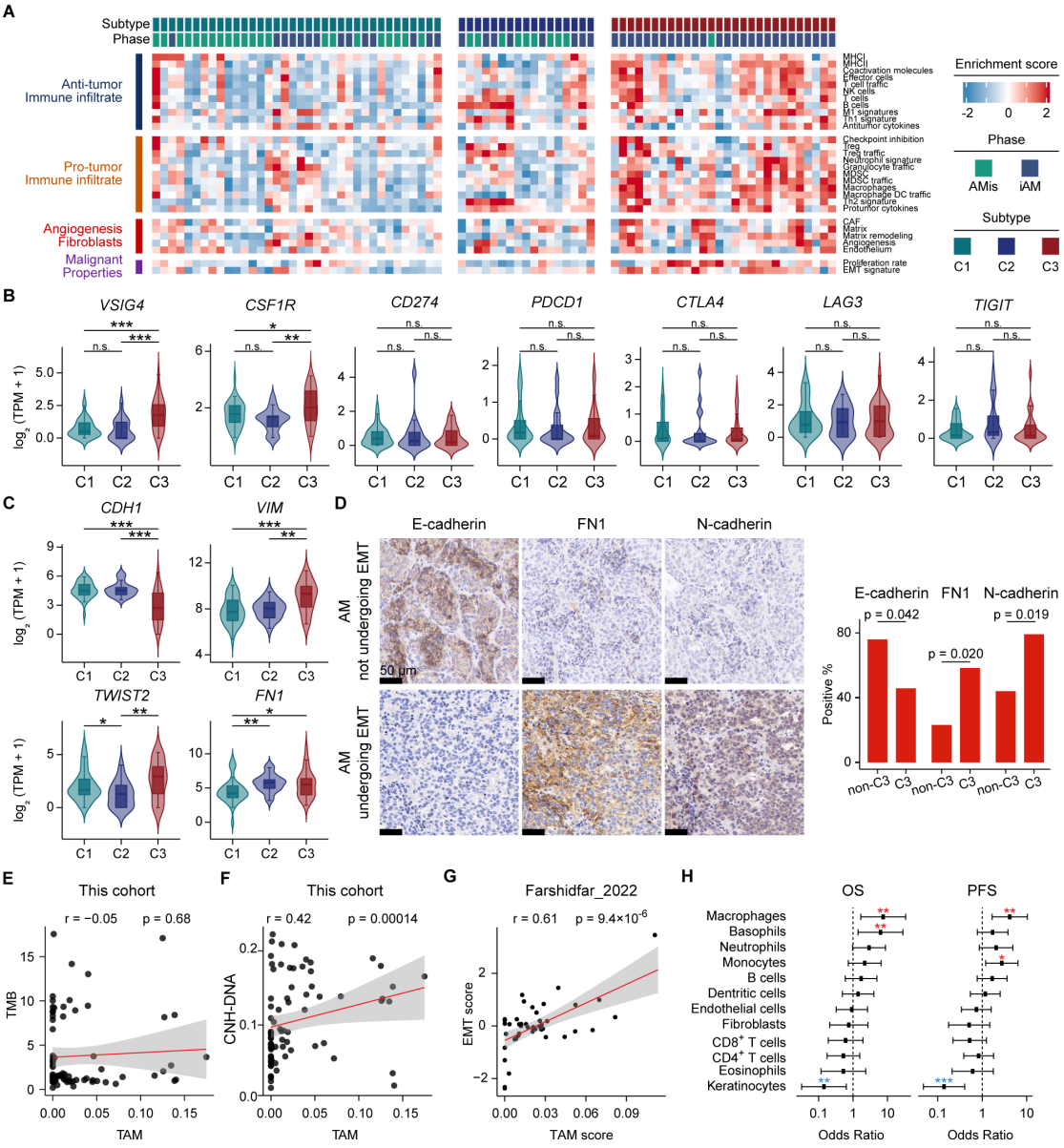

Figure S5. TME signatures and correlation to genomic characteristics, related to Figure 4

(A) Heatmap of 29 TME functional gene expression signatures across three subtypes.
(B) Expression level of immunotherapeutic targets among three subtypes. Mann–Whitney U test.
(C) Expression level of EMT markers across three subtypes. One-sided Mann–Whitney U test.
(D) Representative images showing positive or negative staining of E-cadherin, FN1, and N-cadherin. Scale bar, 50 μm. Statistical results are on the right. Fisher's exact test.
(E and F) Correlations between TAM scores and genetic features, including TMB (E) and CNH-DNA score (F). Spearman correlation test.
(G) Correlation between TAM and EMT scores in the Farshidfar *et al*. cohort. Spearman correlation test.
(H) Forest plots showing the correlation between TME cells and OS (left) or PFS (right) of AM patients based on univariate analyses. Significances for inferior and superior survival are labeled by red and blue asterisks, respectively. Log rank test.

Data are represented as boxplots in (B, C). The centerline shows the median; boxes indicate the first and third quartiles; whiskers extend 1.5 times the interquartile range. *$p < 0.05$, **$p < 0.01$, ***$p < 0.001$.

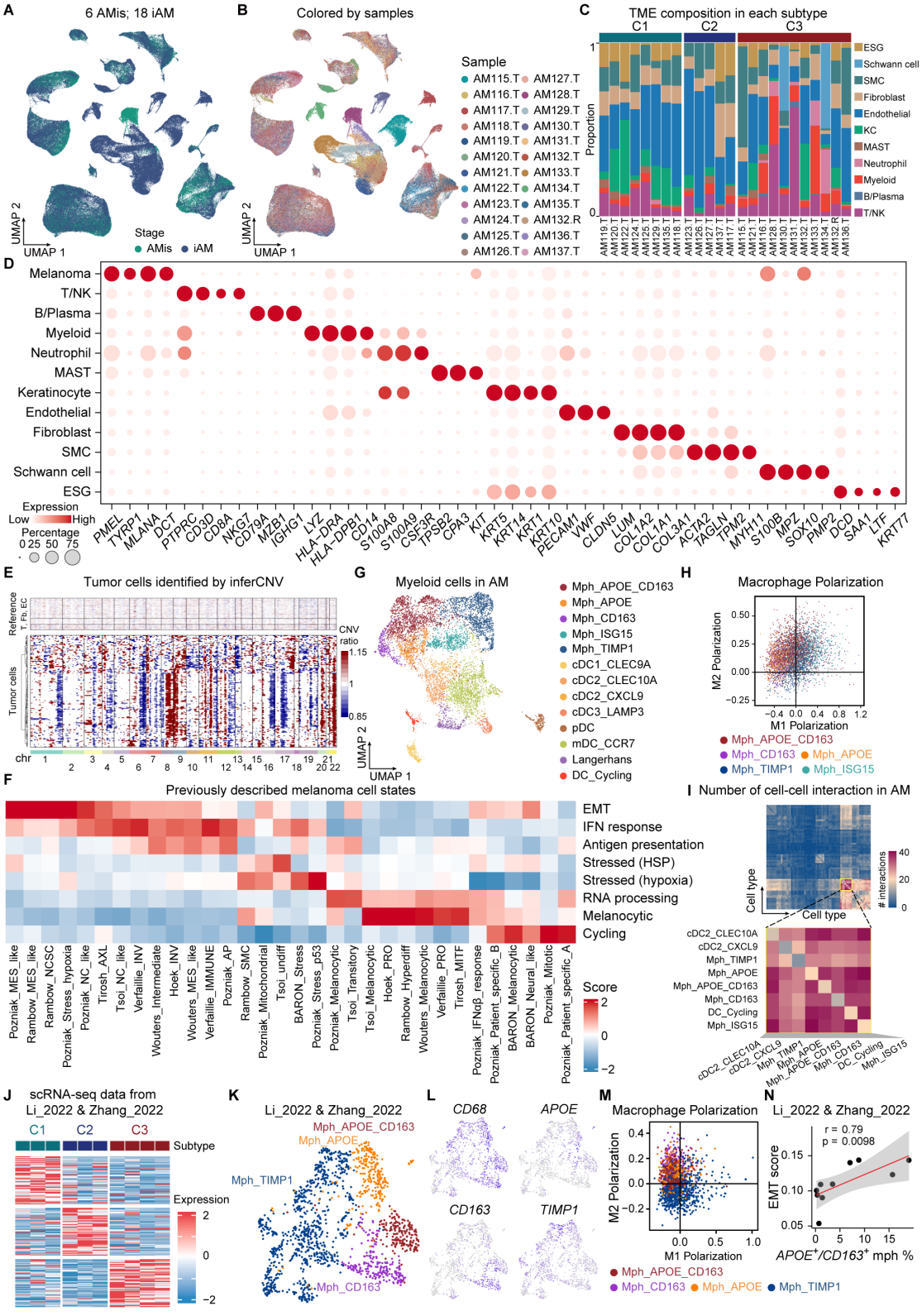

Figure S6. scRNA-seq and subpopulation analysis of AM, related to Figure 5

(A and B) UMAP plot showing all cells labeled by the tumor stage (A) and the identity of samples (B).

(C) Stacked bar plot showing the TME composition in each tumor.

(D) Expression of marker genes for each cell type.
(E) Copy number profile of tumor cells and reference cells (T; Fb, fibroblast; EC, endothelial cell) determined by the inferCNV. Red, amplification; Blue, deletion.
(F) Heatmap showing average scores of previously described CM cell states across each AM cell state.
(G) UMAP plot showing subclusters of myeloid cells.
(H) Scatter plot of macrophage polarization scores of macrophages colored by TAM subclusters.
(I) Heatmap showing the number of cell-cell interactions in AM as determined by CellPhoneDB.
(J) Heatmap showing subtypes of AM patients based on scRNA-seq data from Li *et al*. and Zhang *et al*.
(K) UMAP plot displaying the subsets of macrophages in the AM patients from the public scRNA-seq data.
(L) Expression level of marker genes in macrophages from Li *et al*. and Zhang *et al*.
(M) Scatter plot of macrophage polarization scores of macrophages colored by TAM subclusters annotated in (K).
(N) Correlation between the proportion of $APOE^{+}/CD163^{+}$ macrophages and EMT score in the 10 patients from Li *et al*. and Zhang *et al*. Spearman correlation test.

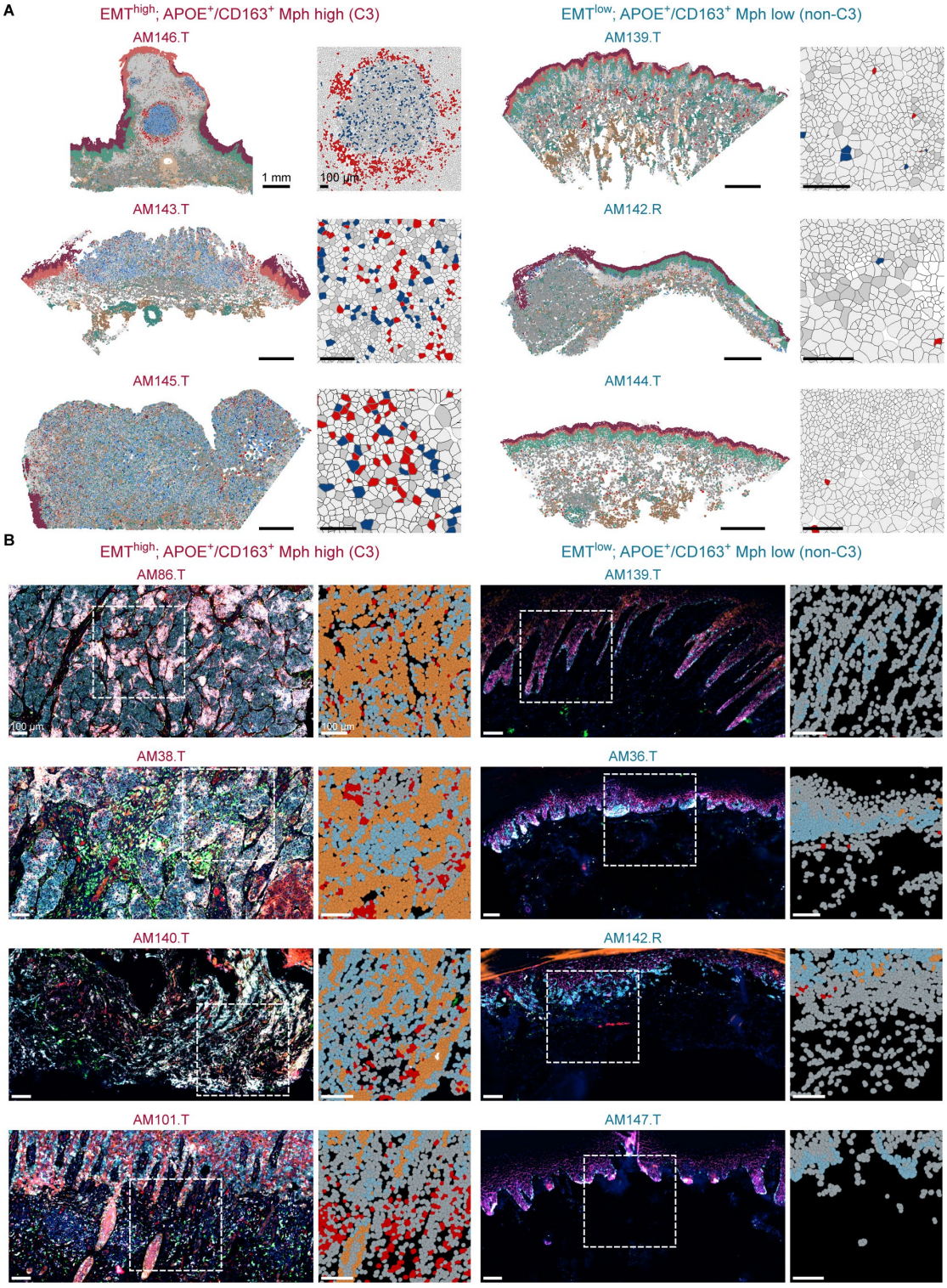

Figure S7. ST and CODEX analyses, related to Figures 6 and 7

(A) Cell segmentation, annotation, and representative spatial distribution of APOE$^+$/CD163$^+$ macrophages (red), EMT tumor cells (blue), other tumor cells (gray), and other cells (white) in ST samples. For each sample, scale bar, 1 mm for full image and 100 μm for enlarged region.

(B) Cell segmentation, annotation, and representative spatial distribution of APOE$^+$/CD163$^+$ macrophages (red), EMT tumor cells (orange), other tumor cells (light

blue), and other cells (gray) in CODEX samples. For each image, the dashed square indicates the enlarged area to the right. Scale bar, 100 μm.

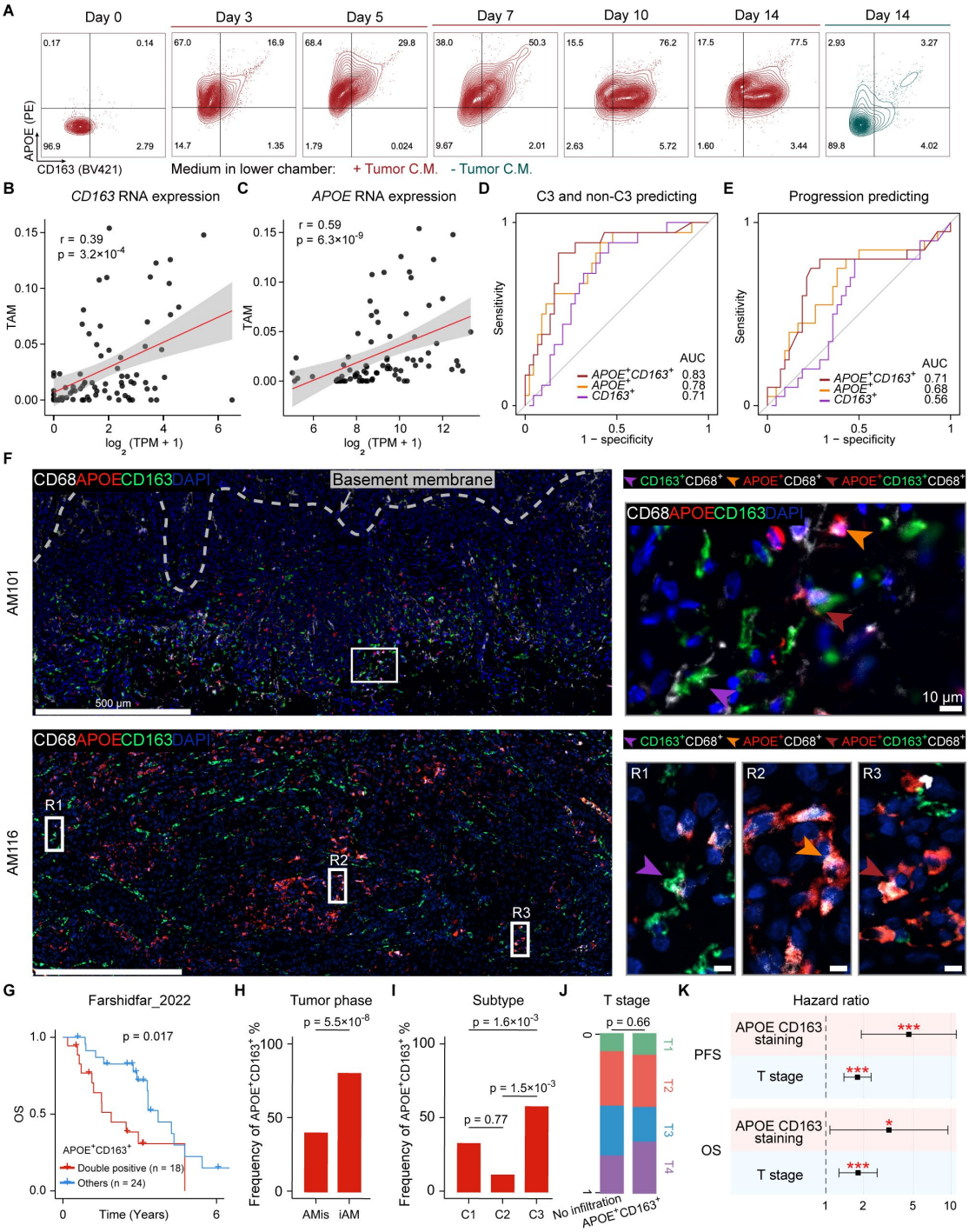

Figure S8. Prognostic values of APOE and CD163, related to Figure 8

(A) Representative flow cytometry plots showing identification of APOE$^+$CD163$^+$ macrophages at different time points.

(B and C) Correlations between TAM score and the RNA expression of *CD163* (B) or *APOE* (C). Spearman correlation test.

(D and E) AUC curves for predicting AM subtypes (D) or progression (E) using the RNA expression level of *APOE* (yellow), *CD163* (purple), and combined *APOE* and *CD163* (red).

(F) The mIHC images of CD68, APOE, and CD163 in patients AM101 and AM116 who were identified as APOE$^+$CD163$^+$ by IHC staining. Area indicated with a square

is enlarged. Gray dashed line, basement membrane. Scale bar, 500 μm (left) and 10 μm (right).
(G) Overall survival, OS, of AM from the Farshidfar *et al*. cohort based on the *APOE* and *CD163* expression. Log rank test.
(H) Fraction of $APOE^{+}CD163^{+}$ patients among two tumor phases. Chi-square test.
(I) Fraction of $APOE^{+}CD163^{+}$ patients across three AM molecular subtypes. Chi-square test.
(J) Stacked bar plot showing the T stage of double positive and no infiltration patients. Chi-square test.
(K) Forest plots showing independent predictive value for PFS (top) and OS (bottom) of AM patients based on multivariate Cox regression analyses in all stained AM patients.